Fabrication of Hollow Silicon Microneedle Arrays for Transdermal Biological Fluid Extraction

by

Hang Zhang

A thesis
presented to University of Waterloo
in the fulfillment of the
thesis requirement for the degree of
Master of Applied Science
in
Electrical and Computer Engineering (Nanotechnology)

Waterloo, Ontario, Canada, 2018

Author's Declaration

I hereby declare that I am the sole author of this thesis. This is a true copy of the thesis, including any required final revisions, as accepted by my examiners.

I understand that my thesis may be made electronically available to the public.

Abstract

This thesis presents the research in the field of microelectromechanical systems with the specific aim of investigating a microneedle based transdermal skin fluid extraction concept. This work presents an innovative double-side Deep Reactive Ion Etching (DRIE) approach for producing hollow silicon microneedle arrays for transdermal biological fluid extraction. The microneedles are fabricated from a double side polished wafer to a shank height of 200-300 μm with 300 μm center-to-center spacing. Moreover, the in vivo testing results are provided as well.

In this thesis, several microfabrication techniques are investigated, developed and applied in the fabrication process. The first chapter brings an overview of nano-/microfabrication and MEMS for biomedical applications (drug delivery and biofluid extraction). Furthermore, the fundamental background of skin structure and interstitial fluid (ISF) is introduced as well. The second chapter clearly illustrates three key techniques specifically employed in the microneedle fabrication process which are photolithography, wet etching and dry etching. The third chapter presents a detailed literature review of microneedles in terms of its general concepts, structures, materials and integrated fluidic system. Eventually, Chapter 4 introduces the details of our method to fabricate hollow silicon microneedle arrays step by step. SEM images and in vivo testing results confirm that hollow silicon microneedle arrays are not only sharp enough to penetrate the stratum corneum but also robust enough to extract ISF out of skin. Ongoing work will focus on the optimization of the assemble extraction apparatus and the capillary filling of the holes.

Acknowledgement

This work was carried out using the nanofabrication facility at Quantum NanoFab, WATLab and Giga-to-Nanoelectronics (G2N) Laboratory at University of Waterloo. Their support is always grateful. The work is partly supported by the NSERC and OCE TalentEdge internship fund. I am greatly acknowledged to ExVivo Labs Inc. for providing me with this precious opportunity.

First, I would like to express my warmest gratitude to my beloved parents for their continuous encouragement throughout my studies. They always encourage and support me behind the scenes so that I can dedicate myself to the research works.

Furthermore, I would like to thank the priceless guidance and suggestions from my supervisor Professor Bo Cui. I am very grateful for getting his kind guidance and invaluable suggestions throughout the entire work.

I also thank to our nanofabrication group at University of Waterloo and R&D team in ExVivo Labs Inc., especially to group mates and co-workers Dr. Y. Li, Dr. R. Yang, Y. Laffitte, U. Schmill, T. Eima, F. Aydinoglu, Y. Liu, M. Soltani and R. Dey.

Table of Contents

List of Figures

Chapter 1 Introduction

This chapter brings an overview of nano-/microfabrication and MEMS for biomedical applications, specially the microneedle-based transdermal drug delivery and skinfluid extraction. Furthermore, the fundamental concept of human skin anatomy and skin interstitial fluid (ISF) is introduced as well.

1.1 Introduction to nano-/microfabrication

A talk entitled ‘There’s Plenty of Room at the Bottom’[1] given by physicist Richard Feynman at an American Physical Society meeting on December 29, 1959, reveals the concepts behind the nanotechnology. Over a decade later, Professor Norio Taniguchi coined the term ‘nanotechnology’ to describe semiconductor processes, while the modern nanotechnology was not begun until the first scanning tunneling microscope (STM) was developed by Gerd Binnig and Heinrich Rohrer in IBM in 1981. Nowadays, nanotechnology is generally defined as science, engineering and technology applied at the nanoscale from 1 to 100 nanometers (nm), involving the capabilities to control individual atoms and molecules. The applications therefore expand diversely in many research areas such as electronics, photonics, biology and medical etc. In particularly, the emerging application of nanotechnologies in medicine and healthcare has increasingly draw attentions in recent years.

Nanofabrication is the design and manufacture of devices with dimensions measured in nanometer. The focus will be primarily on the mechanisms that determine the precision and limitations of nanofabrication technology with an emphasis on those techniques in use for the fabrication of arbitrary shaped structures[2]. In the semiconductor industry, the significant demand of more advanced integration capabilities (e.g., integrated circuit, MEMS and the integration of CMOS/MEMS) constantly improve the development of both microfabrication and nanofabrication technologies, for such development, photolithography and electron beam lithography play an important role respectively. The feature size has shrunk to 500 nm in 1990s and to sub-100 nm in 2000s after the deep UV photolithography was invented in 1982[3]. Figure 1.1 shows the significant improvement in IC technology in last decades. In 2008, the 45 nm generation was developed by Intel conducting immersion lithography, and then in 2009 the 32 nm generation was successfully achieved (White Paper Introducing the 45nm Next-Generation Intel® Core™ Microarchitecture). In April 2012, the 22 nm CMOS process following the 32 nm process was started for CPU products[4]. The TSMC Company began accepting customer tape-outs for its 10 nm FinFET process in the first quarter of 2016.

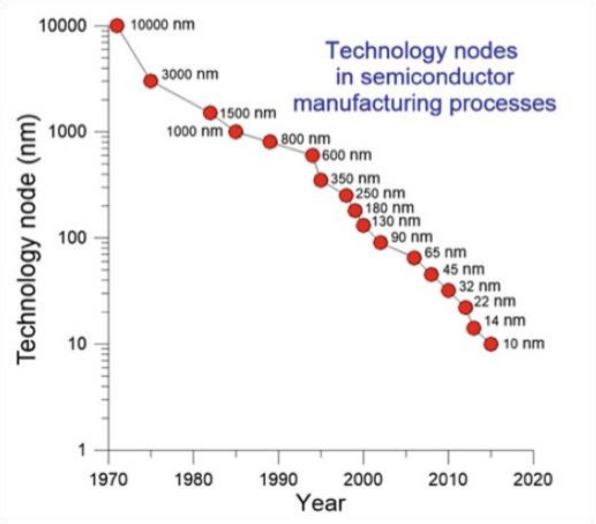

Figure 1.1 Evolution of technology nodes in semiconductor manufacturing processes in log scale[5].

In parallel, innovations in the area of microfabrication have created a unique opportunity for manufacturing micron-sized structures[5]. In order to realize diverse novel applications with ultimate precision and high efficiency, various nano-/microfabrication techniques are carried out in research area, which can be generally divided into two essential approaches: ‘top-down’ and ‘bottom-up’. Top-down methods begin with patterns defined on a relatively larger scale and end up with forming structures in the nm-μm range by reducing its lateral dimensions with lithography techniques such as optical lithography, electron beam lithography (EBL), focused ion beam lithography, nanoimprint and scanning probe lithography. On the other hand, bottom-up methods start with atoms or molecules to build up nanostructures, in some cases through smart use of self-assembly. Figure 1.2 shows the schematic of both the top-down (a) and the bottom-up (b) approaches. In the top-down approach, the resist is first patterned by lithography, and then (1) the pattern is transferred by deposition followed by liftoff, or (2) the pattern is transferred by direct etching. In the bottom-up approach, the pattern is commonly formed by self-assembly and then transferred onto substrates by liftoff[6].

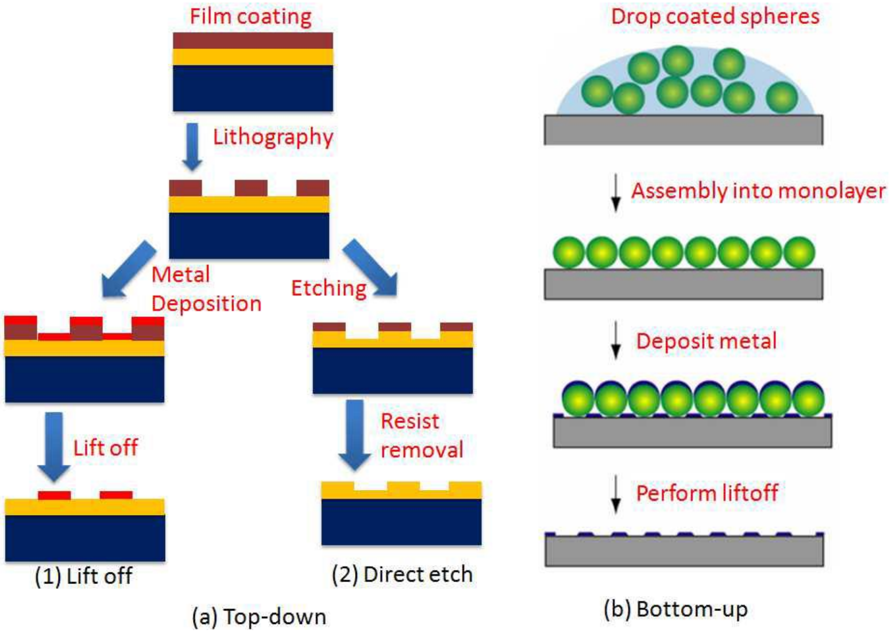

Figure 1.2 Schematic diagram of (a) top-down and (b) bottom-up approach.

Generally speaking, the top-down approach can be subdivided into 3 categories: (a) bulk-/film-machining; (b) surface-machining; (c) mold-machining[6] where most of the key techniques in microfabrication are involved such as lithography, thin-film deposition and etching.

As one of the fundamental and essential techniques in microfabrication, optical lithography is extensively applied and developed from the fabrication of integrated circuits to microelectromechanical systems (MEMS). Lithography techniques will be introduced in detail in the next chapter.

Thin-film deposition as an additive method is crucial to generate the pattern, which is classified into two broad categories: physical vapor deposition(PVD) (sputtering, e-beam or thermal evaporation), and chemical vapor deposition(CVD) (metal-organic CVD, plasma-enhanced CVD or low-pressure CVD). PVD describes a process in which atoms or molecules of a material are vaporized from a solid or liquid source, transported in the form of a vapor through a vacuum or low-pressure gaseous environment, and condense on a substrate[7]. Mechanical, electromechanical or thermodynamic approaches can be exploited during the processes without any chemical reaction involved. CVD is a common industrial process in which the substrate is exposed to one or more volatile precursors that react and/or decompose on the surface to produce the desired deposit. A normal CVD process involves complex fluid dynamics since gases are flowing into the reactor, reacting, and then by-products are transported out of the reactor[8]. The various physical and chemical processes associated with the film growth over the surface in a CVD process are shown in Figure 1.3.

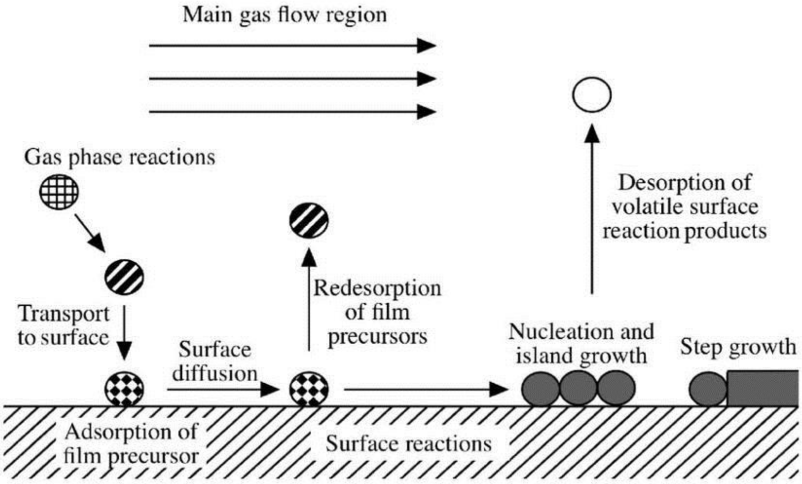

Figure 1.3 An overview of the various stages of film growth over the surface in a CVD process[8].

Etching as a subtractive method is critically important in microfabrication for patterning materials. Etching can be classified into two categories: wet etch and dry etch in terms of two different fundamental types of etchants that are liquid-phase and plasma-phase respectively. Chapter 2 will give a more detailed description of etching techniques.

In addition, bottom-up approach is the other method to be carried out for obtaining the nanostructures (dimensions of typically 2 to 10 nm). The substrate is coated by chemically synthesized nano-particles followed by pattern transfer. Broadly speaking, bottom-up approach should be able to produce devices in parallel and much cheaper than top-down methods, but getting control over the methods is difficult when structures become larger and bulkier than what is normally made by chemical synthesis[9].

1.2 MEMS for biomedical applications

The field of microelectromechanical system (MEMS) was invented initially by the microfabrication techniques discussed above for a variety of applications such as electronics, sensors, actuators[10][11][12]. MEMS devices have critical dimensions in the range of 100 nm to 1000 μm. Therefore, the small size of these devices provides a lot of advantages over large-scale systems in terms of power usage, sensitivity, cost, and space occupation.

At the beginning, MEMS was based on silicon using bulk micromachining and surface micromachining processes[13]. Gradually, some other materials such as polymers, metals and ceramics become common to be applied in the MEMS fabrication. Apart from silicon, polymers can be considered as a good choice for biomedical applications because of its low cost, bio-compatibility and scalability for rapid prototyping.

With the development of microtechnology, various functional MEMS applications have been initiated in daily life. Thus, MEMS technology eventually established itself as a specialized field of study with a significant market share. As a unique, innovative product, the MEMS device has been merged with a variety of fields such as mechanics, fluidics, medical and healthcare. Miniaturized medical wearables and implants, transdermal drug delivery systems, on-chip assays, cell sorting devices, and DNA sequencers are some typical examples of BioMEMS. Figure 1.4 shows the Sensimed's TriggerfishTM wearable MEMS IOP sensor. It consists of a disposable contact lens with a MEMS strain-gage pressure sensor element, an embedded loop antenna (golden rings), and an ASIC microprocessor (2 mm x 2 mm chip).

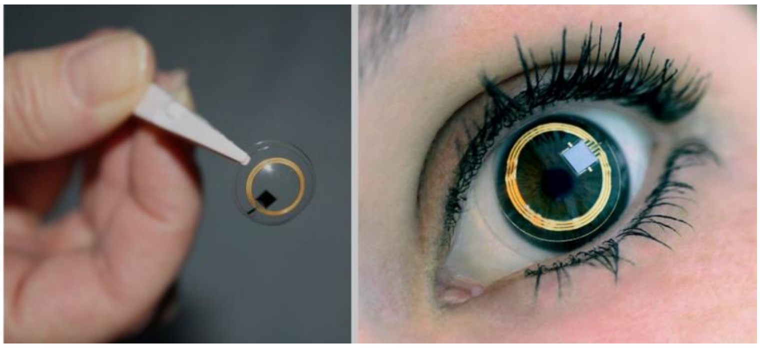

Figure 1.4 Sensimed's TriggerfishTM wearable MEMS IOP sensor[14]. (Source: http://www.sensimed.com/)

Similarly, as one of the typical biomedical applications, MEMS-based microneedles have been used for transdermal drug delivery, blood extraction and bodily fluid sampling. Commonly, solid or hollow microneedles with various shaft shapes are integrated and used in conjunction with microfluidic systems. More details of the microneedles will be introduced in Chapter 3.

1.3 Skin as a barrier

Transdermal patches have been applied for the delivery of drugs that have optimal physicochemical properties which are compatible with stratum corneum such as clonidine, fentanyl, lidocaine, nicotine, nitroglycerin, estradiol, oxybutynin, scopolamine and testosterone[15]. To design microneedles with desired shapes and parameters, some issues such as skin structures, penetration mechanisms and intradermal liquid transport should be figured out first.

1.3.1 Skin anatomy

The skin is the largest organ of the integumentary system[16] and has several functions such as preventing water loss, acting as a nerve sensory ending organ, acting as a site of thermoregulation, etc. It is also a protective membrane that regulates body temperature and fluid loss, guards the underlying muscles and internal organs, and conveys sensory information to the nerve system.

The skin consists of three main layers: the superficial epidermis, dermis and hypodermis as shown in Figure 1.5. The epidermis layer is approximately 50-150 μm thick, forming the outermost skin barrier which is relatively impermeable to both polar and non-polar lithophilic molecules[17]. It is epidermis layer that is optimally targeted for interstitial fluid extraction–superficial enough to be painless. Stratum corneum is the outermost layer of the epidermis, consisting of adherent dead, cornified cells and varying in thickness from 10-40 μm. The epidermis sits atop the lower layer of the skin, the dermis, from which it is separated by a proteinaceous basement membrane[18]. The hypodermis layer (or subcutaneous fat layer) is composed of loose fatty connective tissue and thickness can be different over the surface of the body as well as between individuals.

Microneedle array we designed and fabricated can only penetrate through the outer layer of skin into epidermis layer without interfering with the nerve endings, making minimal invasive injection and extracting ISF out of skin.

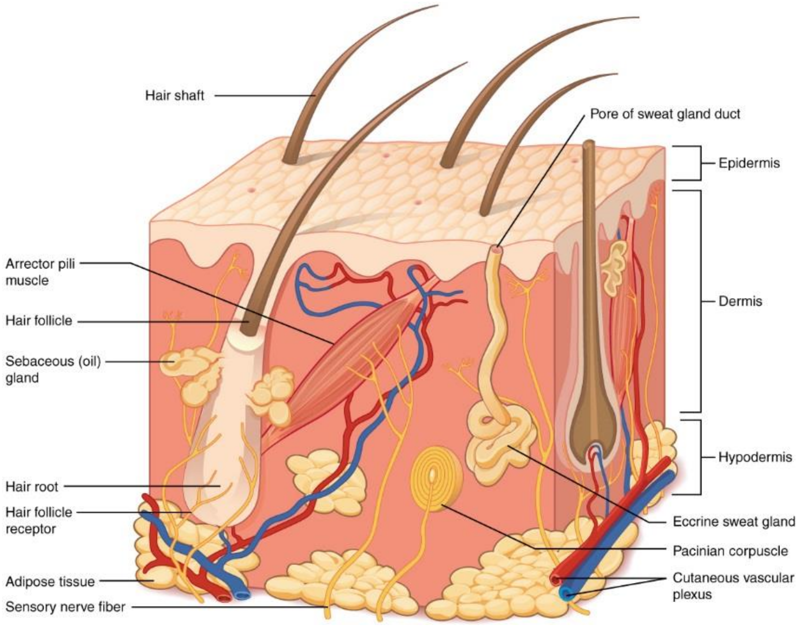

Figure 1.5 Structure of the skin[19].

1.3.2 Interstitial fluid

Interstitial fluid (ISF) or tissue fluid located in the epidermis layer is liquid that surrounds the tissue cells of multicellular animals. Total body water accounts for between 45 to 75% of total body weight in which extracellular fluid (ECF) denotes all body fluid outside the cells. ISF is the main component of the ECF, which constitutes the body's internal environment that bathes all the cells in the body. The extracellular fluid provides the medium for the exchange of substances between the ECF and the cells, and this can take place through dissolving, mixing and transporting in the fluid medium[20].

In March of 2018, new organ termed as 'interstitium' was discovered in the body system after it was previously missed by scientists despite being one of the largest organs in the human body. New analysis published in the journal Scientific Reports is the first to identify these spaces collectively as a new organ and try to understand their function. The newfound organ, beneath the top layer of skin, is also in tissue layers lining the gut, lungs, blood vessels and muscles. The organ is a bodywide network of interconnected, fluid-filled compartments supported by a meshwork of strong, flexible proteins. Figure 1.6 is a schematic summarizing the histological findings.

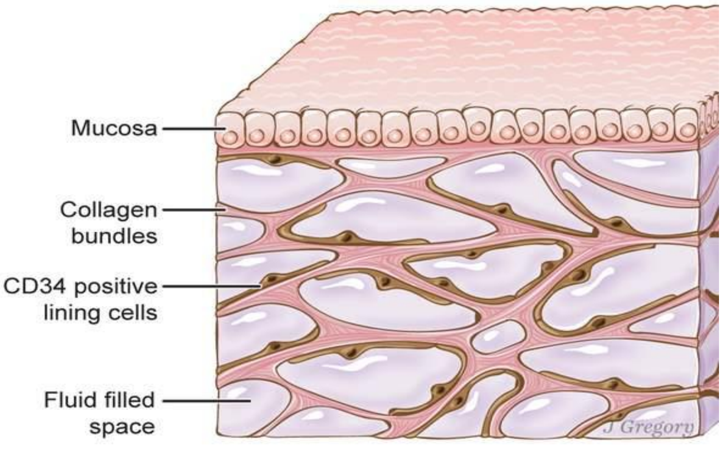

Figure 1.6 Schematic of the fluid-filled space supported by a network of collagen bundles lined on one side with cells[21].

ISF is a proven carrier of several of the most essential biomarkers in the body, which also can be considered as an alternative source of biomarkers compared to blood plasma. It strongly suggests that there is convincing untapped potential for diagnostics area such as allergy testing, drug discovery and scientific research.

Chapter 2 Specific techniques for microneedle fabrication

The fabrication of hollow microneedles is explored and developed by utilizing microfabrication techniques. This chapter illustrates three key techniques specifically employed in the microneedle fabrication process which are photolithography, wet etch and dry etch.

2.1 Photolithography

Developed in 1959, photolithography is a process that adopts high-intensity UV light and a photomask to prepare a polymer pattern on a silicon wafer[22][23]. As a well-established method commonly applied in the semiconductor industry today, photolithography, the underlying process for the fabrication of these complicated electronic devices, is rooted in MEMS technology. Much of today's information technology counts on microchips that are designed and fabricated by microfabrication techniques. It facilitates circuit integration, through patterning and etching the multiple device layers, and creating vias and interconnects with modest alignment tolerances[24]. Figure 2.1 shows the picture of a lithography system we used in University of Waterloo for alignment and UV exposure of resist-coated wafers.

Figure 2.1 MA/BA6 Mask and Bond Aligner (Courtesy to SUSS MicroTec).

The basic photolithography process is employed to selectively remove parts of a thin film (or the bulk of a substrate) by changing the chemical structure/solubility of the photoresist that contains a light-sensitive compound and a mixture of polymers. A geometric pattern is eventually transferred from a photomask to a photoresist on the substrate. There are two types of photoresists. If a positive photoresist is exposed, the illuminated area becomes highly soluble during development, while a negative photoresist is composed of monomers or polymers that polymerize or crosslink to form insoluble polymers upon ultraviolet (UV) exposure. Hence various required structures can be defined perfectly and efficiently by coating different types of photoresists.

As shown in Figure 2.2, it usually starts with depositing (e.g. spin coating) photoresist onto a substrate followed by soft baking to evaporate the solvent inside. A photomask with the desired structural feature is well positioned above the photoresist using a mask aligner, then UV light travels through and focuses on the photoresist layer that is going to be soluble or insoluble depending on which type of photoresist spun onto the substrate. Diverse exposure modes can be determined upon UV exposure such as soft contact, hard contact, proximity and projection mode. For positive resist, the area covered by dark area of the mask still stays insoluble; on the contrary the exposed area will be dissolved during subsequent development, leaving behind a patterned layer of photoresist. This defined pattern will act as a barrier to protect the underlying film from wet or dry etching in the following process. Ultimately, the pattern is transferred from a photomask to the substrate successfully.

In conclusion, conventional photolithography can only achieve a resolution around 1 μm, but many resolution enhancement techniques (RET) have been studied over the years such as off-axis illumination (OAI) and phase shift masks (PSM), leading to a resolution down to less than 10 nm. In this project, photolithography is a key step to transfer the pattern from photomask we designed to photoresist AZ4620 followed by wet or dry etching to define pillar and hole structures.

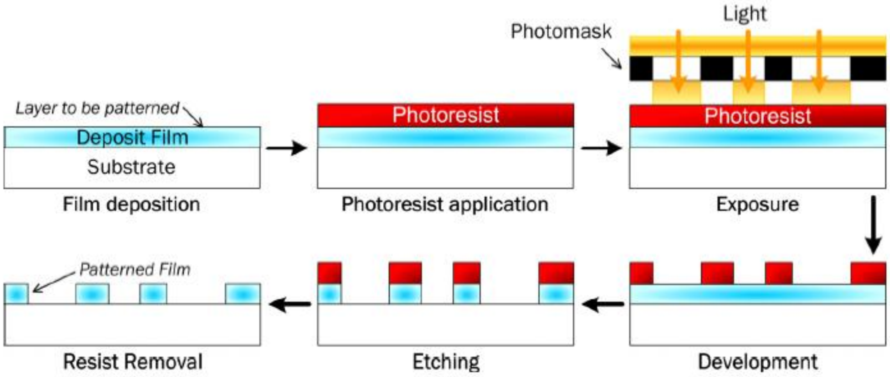

Figure 2.2 Basic photolithography process using positive photoresist: the exposure and etching process that allows one to transfer a pattern to the film/wafer[24].

2.2 Etching

As a pattern transfer method, etching is a critically essential process to selectively remove layers from the surface of a wafer resulting in desired patterns. A photoresist that has been patterned using lithography can be utilized as the masking material to protect the wafer from the etchant. It is frequently used in the microfabrication processes of semiconductor devices for the purposes of wafer planarization, isolation and cleaning.

There are several important metrics in the etching process such as uniformity, etching rate, selectivity, anisotropy and undercut. Etching rate is defined as etched depth per unit time, normally influenced by the concentration of the etchant and temperature. Figure 2.3 shows that silicon etching rates in [nm/h] depend dramatically on KOH concentrations and etch temperatures. Selectivity is defined as the ratio of the etching rate between different materials. To define a high aspect ratio structure such as deep holes and high pillars, the masking material is supposed to have high selectivity to protect the underlying film. Figure 2.4 illustrates the poor selectivity resulting in defects during etching process. Anisotropy or isotropy is another critical parameter discussed often in the etching process. Figure 2.5 shows the difference between isotropic (uniformly in all directions) and anisotropic etching (etches in vertical direction).

Etching can be classified by two fundamental categories based on the type of the etchant: wet etch (liquid-based etchants) and dry etch (plasma-based etchants). Wet etch is easily implemented by immersing the wafers in a chemical solution with quick reaction, but it is quite hard to control and define the precise feature sizes that are smaller than 1 μm, as well as producing chemical waste. On the other side, dry etch, also called plasma etching, reactive ions in a gas phase are formed in a vacuum system to sputter or dissolve the materials, which is more accurate and controllable compared to wet etch. Furthermore, dry etch is capable to obtain 100nm feature size. In our microneedle fabrication process, both dry etch and wet etch are performed in the experiments.

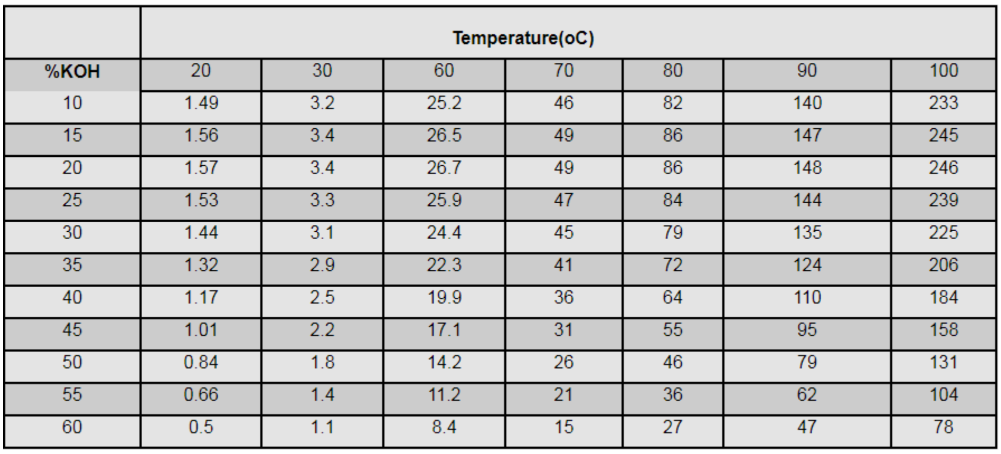

	Temperature(oC)						
%KOH	20	30	60	70	80	90	100
10	1.49	3.2	25.2	46	82	140	233
15	1.56	3.4	26.5	49	86	147	245
20	1.57	3.4	26.7	49	86	148	246
25	1.53	3.3	25.9	47	84	144	239
30	1.44	3.1	24.4	45	79	135	225
35	1.32	2.9	22.3	41	72	124	206
40	1.17	2.5	19.9	36	64	110	184
45	1.01	2.2	17.1	31	55	95	158
50	0.84	1.8	14.2	26	46	79	131
55	0.66	1.4	11.2	21	36	62	104
60	0.5	1.1	8.4	15	27	47	78

Figure 2.3 Silicon etching rates in [nm/h] for various KOH concentrations and etch temperatures(Courtesy to Nanosystem Fabrication Facility)[25].

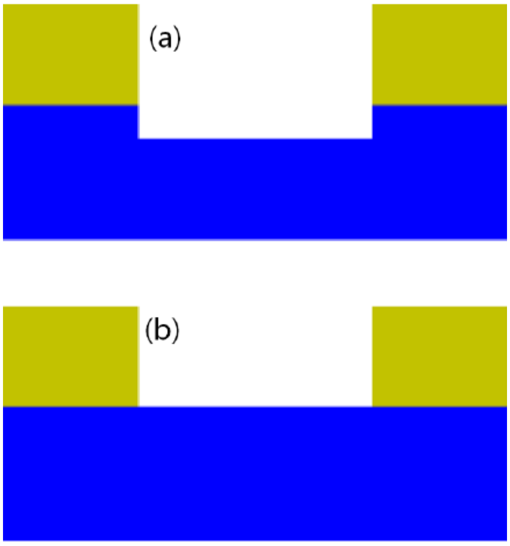

Figure 2.4 A graphical representation of (a) a poor selectivity that causes the etchant to attack the bottom layer material while removing the top layer, (b) a high selectivity that results in etching out the top layer without affecting the underlying layer[26]. (Courtesy to Smack.)

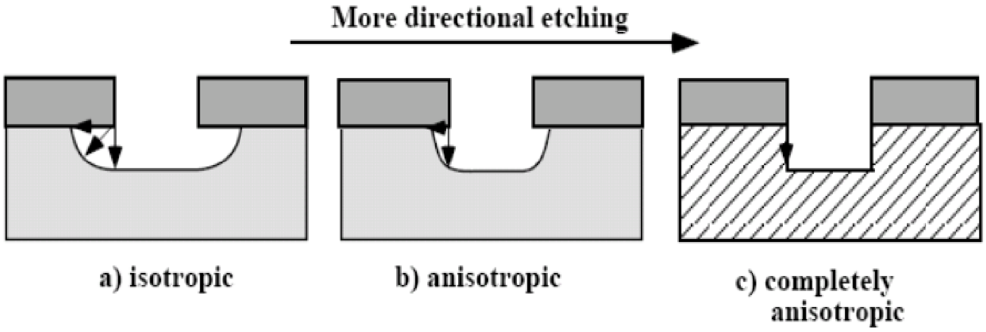

Figure 2.5 A schametic of (a) Isotropic etching of silicon (b) Partially anisotropic (c) Completely anisotropic [27] (Courtesy to Mikael Östling.)

2.2.1 Wet etching

As mentioned above, wet etching is referred to as an etching process of solid materials in a chemical solution which the substrate is dipped in or sprayed on. It is extremely efficient for etching silicon, oxide, and metals into a relatively large feature size with some dimension loss. Normally several chemical reactions get involved in a single wet etching process that consumes the original reactants and produces new reactants.

Three key steps in the wet etching process are shown in Figure 2.6: (1) Liquid etchant will be diffused to the surface to be etched. (2) Chemical reactions will happen at the surface. (3) Byproducts from the surface will be removed by diffusion. Good etching uniformity and consistent etching rate are important in the wet etching, thus nowadays spray etching is progressively applied in industry over immersion etching.

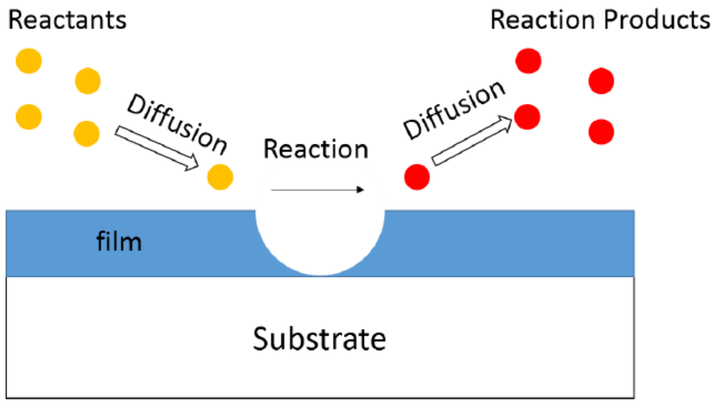

Figure 2.6 A schematic of wet etching process: the diffusion of the reactants to the reacting surfaces, the chemical reaction at the surface and the transportation of the products away from the surface by liquid flow[28].

Both anisotropy and isotropy can be achieved by wet etching. Alkaline liquid solvents, such as potassium hydroxide (KOH), ethylenediamine pyrocatechol (EDP), or tetramethylammonium hydroxide (TMAH) are common anisotropic etchants to etch bulk silicon because the etching rate varies dramatically on different silicon crystalline planes. Figure 2.7 shows the three major planes in a cubic unit silicon termed as <111>, <100>, <110> by Miller index. Less available bonds per unit area are presented in the <111> plane than the other two planes, thus the etching rate is expected to be slower for the <111> plane[29].

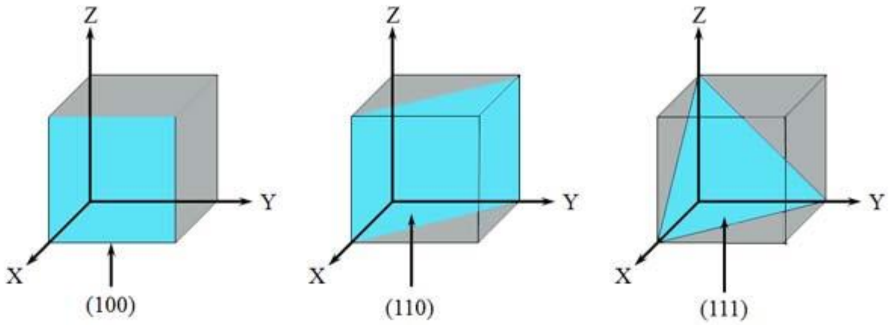

Figure 2.7 A graphical representation of silicon crystal planes. (Courtesy to Crystal Scientific.)

Based on the etching rate ratio between the crystal planes in the silicon lattice, silicon microneedle structures with high accuracy and good reproducibility can be fabricated by using KOH wet etching technology. A research group in Tyndall National Institute established a systematic method of microneedle manufacturing with well-defined structures in 2005[30]. Figure 2.8 shows the process flow chart starting from a standard, P-type, bare silicon wafer with <100> orientation. As it is shown, wet etching of silicon microstructures with high index crystal planes forming microneedle shapes is exploited by using 29% KOH and a temperature of 79 °C. Step 3 illustrates the formation of <111> silicon crystal planes. After a certain etch depth, <111> crystal planes are etched away by faster etching planes (etch rate > 1.3 μm/min), with an octagon at the base. The needle shape is defined by the eight high index crystal planes, defined as <312> planes[30]. Figure 2.9 presents the result of one single microneedle shape with a height of 280 μm.

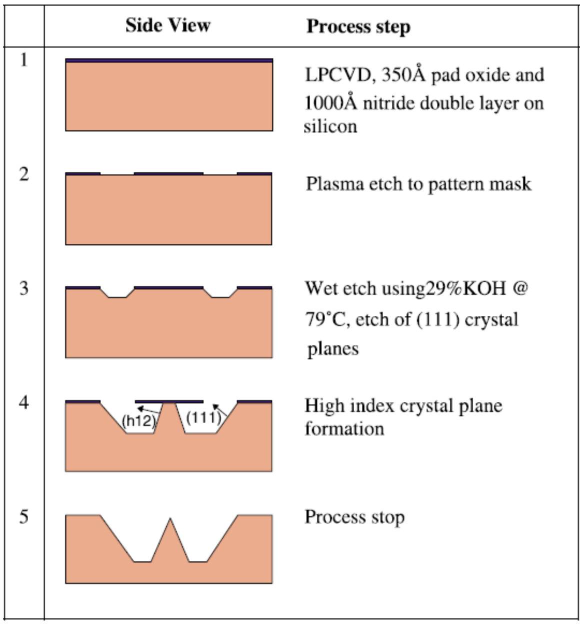

	Side View	Process step
1		LPCVD, 350Å pad oxide and 1000Å nitride double layer on silicon
2		Plasma etch to pattern mask
3		Wet etch using29%KOH @ 79°C, etch of (111) crystal planes
4		High index crystal plane formation
5		Process stop

Figure 2.8 Wet etch process flow from N. Wilke's research group. (Courtesy to N. Wilke, A. Mulcahy, etc.)

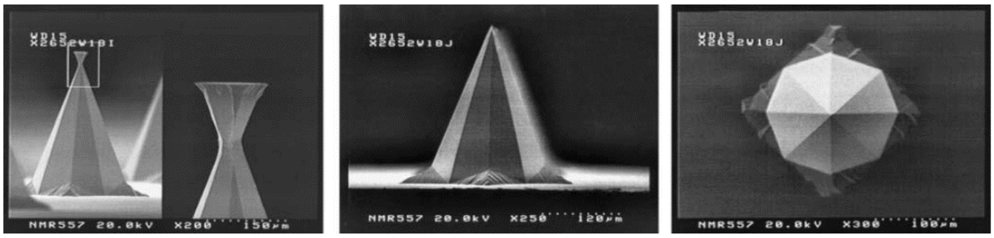

Figure 2.9 SEM picture of a single microneedle from N. Wilke's research group: side view with detail of negative slope etch (left); side view (middle); top view (right). (Courtesy to N. Wilke, A. Mulcahy, etc.)

On the other side, isotropic wet etching of silicon with HF-HNO_3 mixtures is widely used in today's semiconductor industry and in the production of solar cells. For example, an isotropic silicon etchant composed of hydrofluoric, nitric and acetic acids (replaceable with water), commonly called HNA, has a fast, yet very reproducible etch rate of degenerately doped, p-type silicon[17]. This etching mechanism was done by Robbins and Schwartz. Figure 2.10 shows the etching rate of silicon. The solid curves correspond to the etching system in which acetic acid is the diluent, whereas the dashed curves correspond to the system in which water is the diluent[31]. The reaction can be divided into two simultaneous steps: (a) oxidation of silicon into silicon dioxide (SiO_2) by HNO_3 (Eq. (2.1)) and (b) SiO_2 removal using HF (Eq. (2.2)). The overall reaction is given in Eq. (2.3). It is important that the etching rate is limited by the rate of oxide removal. HF diffusion to the silicon surface will be the rate-limiting factor, which will result in faster etching (shrinking) of the pillar top.

$$3\mathrm{Si} + 4HNO_3 \rightarrow 3SiO_2 + 4NO + 2H_2O \qquad \text{Eq. (2.1)}$$

$$SiO_2 + 6\mathrm{HF} \rightarrow H_2SiF_6 + 2H_2O \qquad \text{Eq. (2.2)}$$

$$3\mathrm{Si} + 4HNO_3 + 18HF \rightarrow 3H_2SiF_6 + 4NO + 8H_2O \qquad \text{Eq. (2.3)}$$

In terms of R. Bhandari's research on a wafer-scale etching technique in 2010, two-steps etching was introduced: (1) dynamic and (2) static etching[32]. Figure 2.11

illustrates the etching progression combined with dynamic and static etching.

Based on the theories above, in this work, a static wet etching system made up of the mixed solution HF (49%)–HNO_3 (69%) in a ratio of 1:19 by volume was set up to sharpen silicon pillars into a sharp needle-shaped profile.

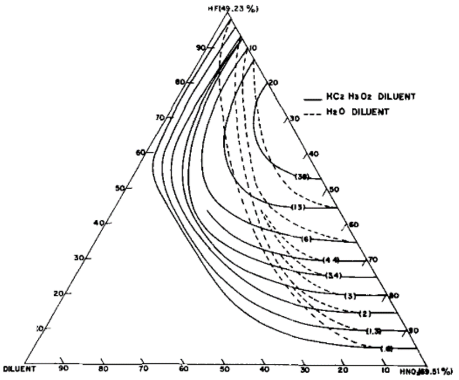

Figure 2.10 Curves of constant etch rate of silicon (mils/min) as a function of etchant composition in the system 49% HF, 70% HNO_3, and diluent[31].

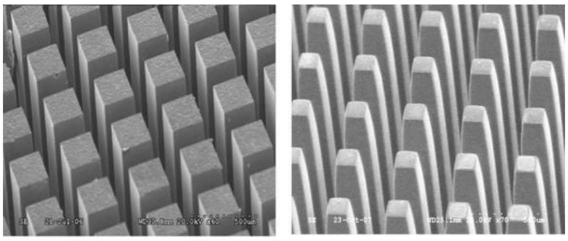

(a): After dicing (b): After dynamic etching (t = 4 min)

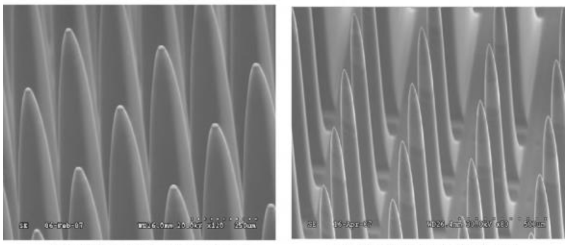

(c): During static etching (t = 7 min) (d): After static etching (t = 8 min)

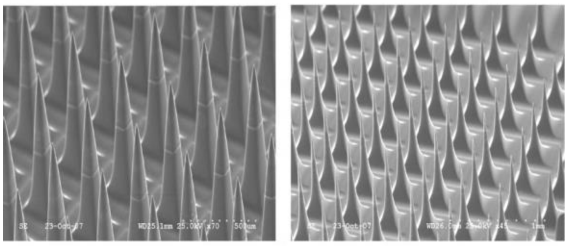

(e): After static over-etching (t = 8.3) (f): After static over-etching (t = 9 min)

Figure 2.11 SEM images showing progress of needle formation from dicing through etching (a–f). The rectangular columns (a) are transformed into sharp needle shapes (d) during static etching (8 min). The high etch rate (20 µm/min) causes change in the geometry[32]. (Courtesy to R. Bhandari, S. Negi, etc.)

2.2.2 Dry etching

Dry etching is an essential process step that is widely used in the fabrication of microelectromechanical systems (MEMS). In today's semiconductor manufacturing, it is easier to control and capable of defining feature sizes smaller than 100 nm compared to wet etching which is strongly affected by ambient parameters like temperature and humidity. Plasma is a fully or partially ionized gas composed of equal numbers of positive and negative charges, as well as some neutral molecules. Electrons can be accelerated to gain energy to form plasma as a high energetic condition in which many processes can take place. Dry etching was introduced in late 1970's.

Dry etching may remove the materials by chemical reactions, by purely physical methods, or with a combination of both chemical reaction and physical bombardment. Thus, it is usually classified into three main categories: (1) the chemical plasma etching (PE), (2) the synergetic reactive ion etching (RIE) and (3) the physical ion beam etching (IBE). Figure 2.12 shows the typical products of the three basic mechanisms of dry plasma etching. PE gives rise to isotropic profiles, high etch rates and high selectivity, whereas IBE presents positively tapered profiles, low selectivity and low etch rates. RIE enables the achievement of profile control due to the synergetic combination of physical sputtering with chemical activity of reactive species with high etch rate and high selectivity[33].

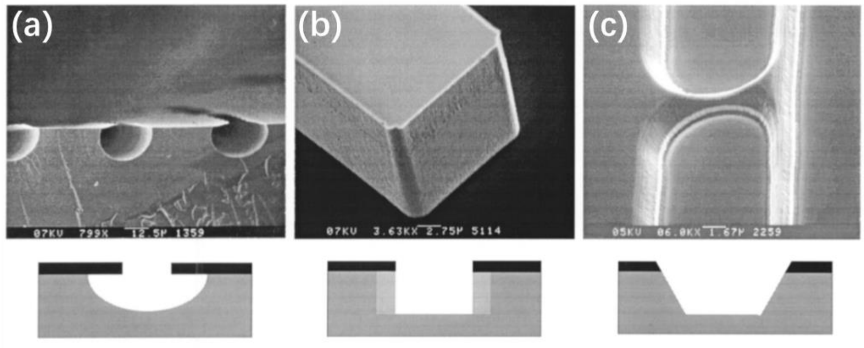

Figure 2.12 Typical etching profiles of the three basic mechanisms of dry plasma etching. (a) the chemical plasma etching (PE), (b) the synergetic reactive ion etching (RIE) and (c) the physical ion beam etching (IBE). (Courtesy to H. Jansen, H. Gardeniers, etc.)

If the etching relies only on ion bombardment, it is not efficient and very time-consuming. Thus, Reactive Ion Etch (RIE) has been considered as a very popular etch technique combining physical process with chemical reactions to improve the etch rate. Technically, the function of the ion bombardments is to enhance surface adsorptions, etching reactions, or byproducts removal. Figure 2.13 compares the silicon etch rates for applying different gas phase with or without the aid of Ar ion beam. Very slow etch rate will be achieved by pure chemical or physical dry etch alone, while ion-assisted chemical etch is a lot more efficient.

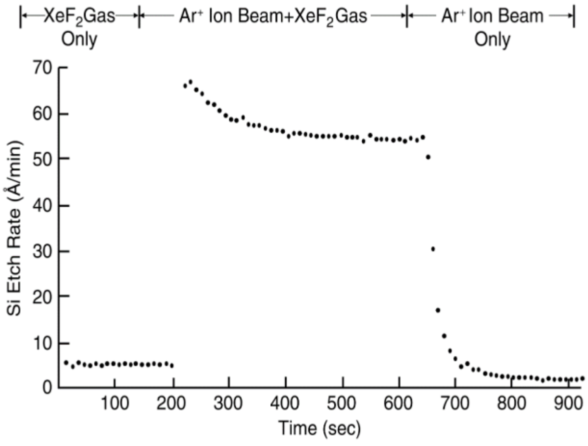

Figure 2.13 Etch rates of silicon as only XeF_2 gas, only Argon ion beam, and combination of them are introduced to the silicon surface. Ion-assisted chemical etch undoubtedly boosts the efficiency of the etching.

The mechanism of RIE can be divided into four steps as shown in Figure 2.14.

Firstly, a feed gas is introduced into the chamber, where it is broken into chemically reactive species, which diffuse through boundary layer and along surface of wafer. Both neutral radicals and ions are generated in the plasma at first. Once the reactive species reach the surface, thermally activated reaction will produce soluble species. Eventually, the etching product will desorb from the wafer surface and diffuse away through the gas steam.

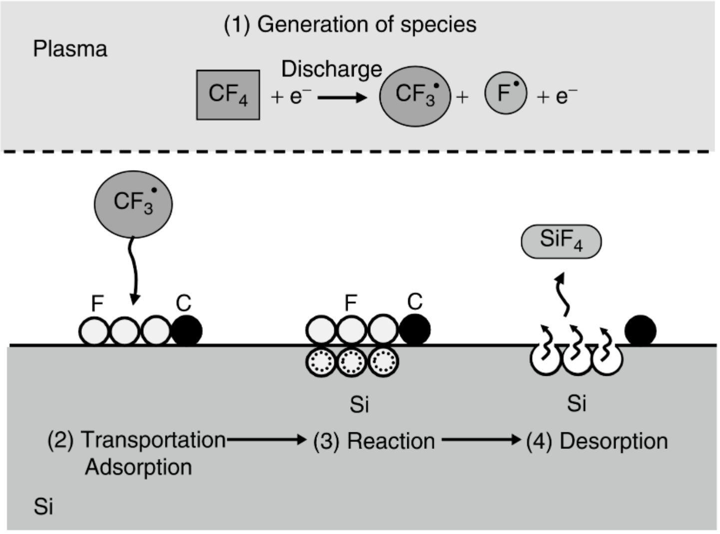

Figure 2.14 Reaction steps of RIE for the case of Si etching by using CF_4[34][35].

Even if directional ion bombardments with low density are applied in the process, some isotropic etching may still exist especially when it comes to the microstructures with high aspect ratio. To obtain high etch rate, high aspect ratio and vertical sidewalls, Deep Reactive Ion Etching (DRIE) through the so-called Bosch process has become a competitive technology for high volume MEMS fabrication.

DRIE etches vertically into the silicon wafer with high selectivity, producing structures in the silicon with vertical profiles and high aspect ratios. This is achieved without degrading the desired structures from etching in the lateral direction. For the Bosch process, there are two different plasmas that exist in the chamber, which involves a sequence of alternating steps of etching and protective polymer deposition (referred together as “cycles”), switching within seconds. The details are shown in Figure 2.15 step by step. In the etch step, SF_6 will react with silicon first to produce SiF_4 which is gaseous and pumped out of the system by the vacuum pump. Each etch step provides a short period of high rate isotropic (i.e. non-directional) silicon removal, which is normally less than one micrometer deep. It is followed by the deposition step that generates a passivating polymer film that protects lateral etching of the exposed silicon sidewalls during subsequent etching cycles. The C_4F_8 decomposes in the plasma and forms chains of a Teflon-like polymer that will not react with the etch plasma to protect the covered silicon from being further etched. Ions in the plasma can be accelerated in the electric field to physically and directionally sputter away the polymer on horizontal surfaces. The polymer will not be removed from the sidewalls and left there to protect the profile when the reactive part of the etch takes place. By switching back and forth between etch and deposition plasmas the silicon is etched in an anisotropic fashion to the desired etch depth[36]. In addition, the etch rate of the Bosch process is dependent on the percentage of exposed silicon on the wafer to be etched. Figure 2.16 shows the etch rate curve in terms of the standard Bosch process at University of Alberta. In our work, standard Bosch process recipe developed at the NanoFab at University of Waterloo is performed to produce ~350 μm deep holes and ~300 μm high pillars. The etch rate is around 400 nm/cycle and uniformity is approximately 2%.

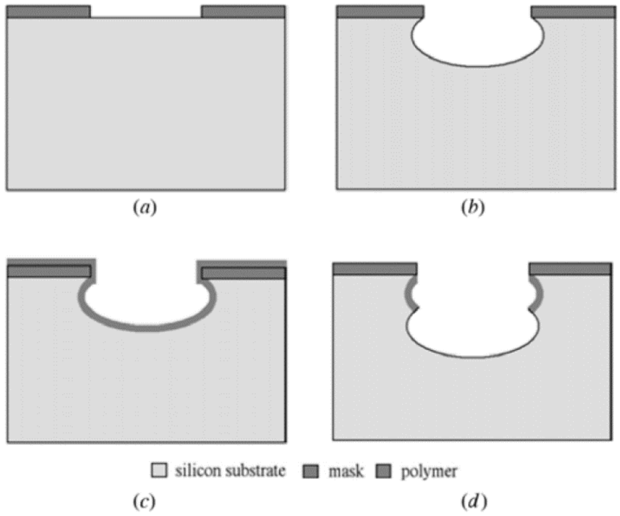

Figure 2.15 A schematic of the principle of the Bosch process[37]: (a) Sample with mask (b) First etch step (c) Deposition Step (d) Second etch step.

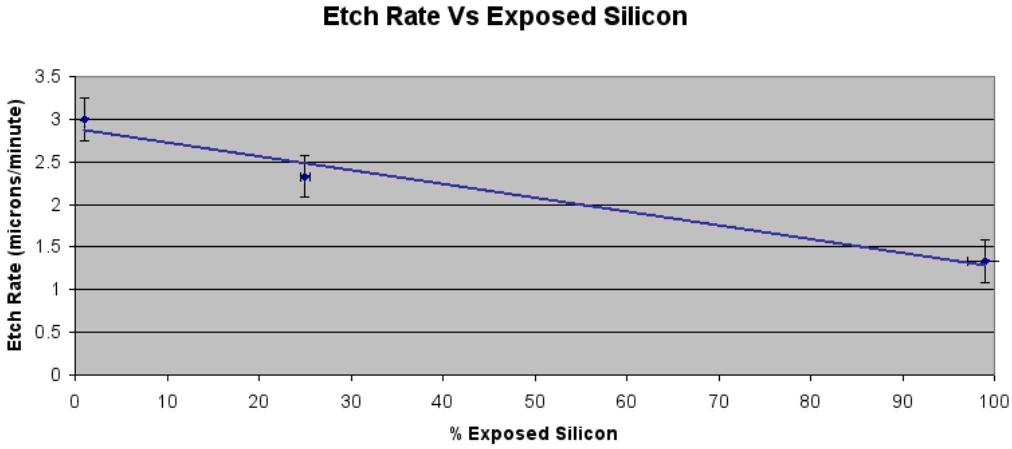

Figure 2.16 Etch rate curve related to the amount of exposed silicon[36].

In conclusion, wet etch is easily implemented in the experiment with quick reaction, but it is quite hard to control and define the precise feature sizes that are smaller than 1 μm. On the other hand, dry etch like DRIE process itself is an established methodology to create structures (pillars and holes in our work) with high aspect ratio, but developing an optimized recipe for successful etching of hollow microneedles is a significant challenge. In our work, both dry etch and wet etch are exploited in the experiments.

Chapter 3 Overview of microneedles

This chapter gives a detailed literature review of microneedles in terms of its general concepts, structures, materials and integrated microfluidic system.

3.1 Application of microneedles

Oral administration of drugs was considered as a conventional drug delivery method in the past, but some drawbacks came out gradually because such techniques are often not applicable for new protein based, DNA-based, and other therapeutic compounds produced by modern biotechnology[38][39][40]. Applying transdermal patches to deliver drugs across the skin becomes an attractive approach for the patients who are suffering painful injection via a hypodermic needle. However, transdermal delivery, which relies on drugs passively diffusing across the skin, is severely restricted and hindered by the low permeability of the outer 10-20 μm of skin, the stratum corneum layer[41][42].

To increase skin permeability and reduce the pain simultaneously, the idea of combining the benefits of needle injection and transdermal patches is brought out, resulting in the creation of the microneedle concept. This concept involves micron-size needles that have representative parts with generally hundreds of microns long, few to tens of microns wide at the tip, and on the order of 100 μm wide at the base[15]. Such microneedles are appropriately long to penetrate through the outer layer of skin without interfering with the nerve endings in the deeper layer, enabling minimal invasive and painless sampling. Some of the basic designs and materials used to fabricate microneedles are introduced below.

3.2 Silicon microneedle structures

Over the past few years, extensive research has been performed on a variety of different microneedle designs and fabrication methods. Various microneedle structures have been designed for assorted applications such as the applicators for transdermal drug delivery and biosensors for extraction of biofluids.

Silicon microneedles can have solid or hollow structures, and can be classified into two models as well based on the fabrication process: in-plane or out-of-plane microneedles.

The orientation of in-plane and out-of-plane microneedles is completely different. In-plane needles are arranged along the plane of the substrate while out-of-plane needles are set up perpendicular to the plane of the substrate. Figure 3.1 presents (a) 6 mm long in-plane microneedle and (b) 1.5 mm long out-of-plane microneedles respectively.

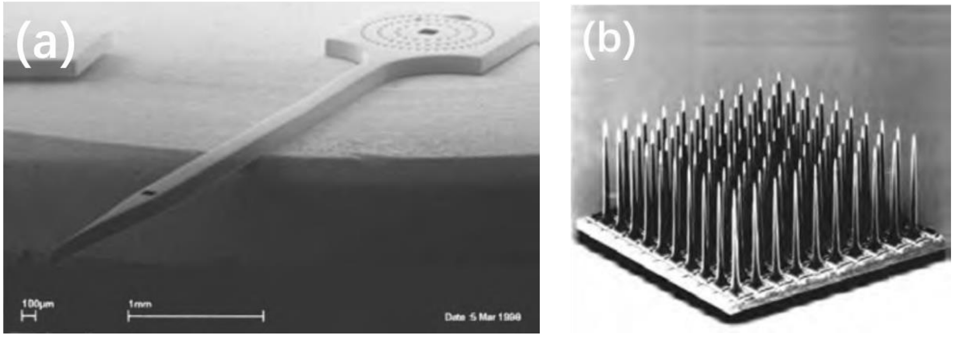

Figure 3.1 (a) 6 mm long in-plane silicon microneedle with embedded fluidic channels[43]. (Courtesy to Talbot and Pisano) (b) Individually addressable, 1.5 mm long, solid, sharpened to point, out-of-plane microneedles used as neural electrodes[44]. (Courtesy to Campbell et al.)

Early microneedles were in the form of solid microneedles. They are designed to increase the skin permeability by piercing the stratum corneum to create micron-size openings that allow molecular transport across the skin, or alternatively to expose the underlying skin layers to the drugs that already coat on the surface of the needles[45]. Solid microneedles tend to be simpler to fabricate compared to hollow microneedles[15]. Figure 3.2 (a) shows that the first out-of-plane solid microneedles for transdermal drug delivery applications[46][47].

In contrast to solid microneedles, hollow needles not only offer the feasibility of active injection into the tissue, but also present the successful extraction of biofluid from the skin. The first hollow out-of-plane microneedles were produced by McAllister et al. in 1999[47]. Figure 3.2 (b) shows that 150 µm long hollow silicon microneedles can be fabricated by combining the fabrication process of solid silicon microneedles with DRIE Bosch process to form a needle bore[47][48].

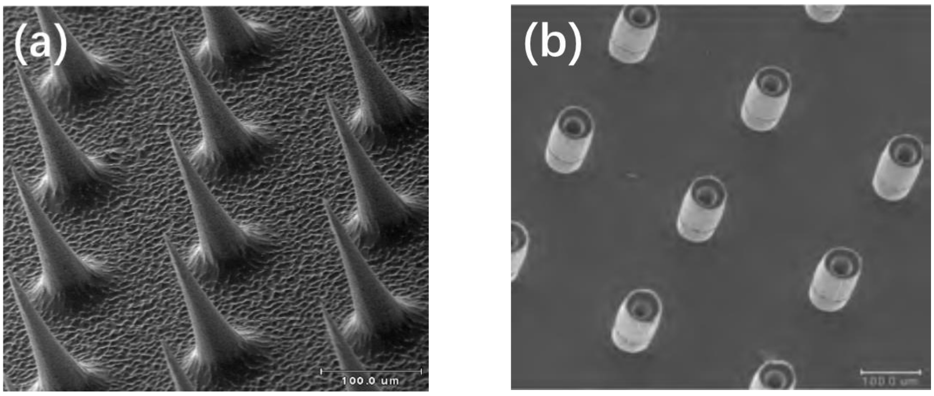

Figure 3.2 (a) Solid silicon microneedles used for transdermal drug delivery. Approximately 80 μm at the base and 150 μm long solid microneedles were fabricated in silicon using DRIE, and featured sharp tips with a tip radius below 1 μm[46]. (b) The first hollow out-of-plane microneedles by McAllister et al. The silicon needles are 150 μm long and were fabricated through DRIE using the Bosch process[48].

In 2000, Stoeber and Liepmann together created another type of hollow silicon microneedles[47][49]. The needle bores are produced from the backside DRIE process and needle shape is etched from the frontside of the wafer by isotropic dry etching. Figure 3.3 shows hollow silicon microneedle array with (a) pointed tip and (b) flat tip.

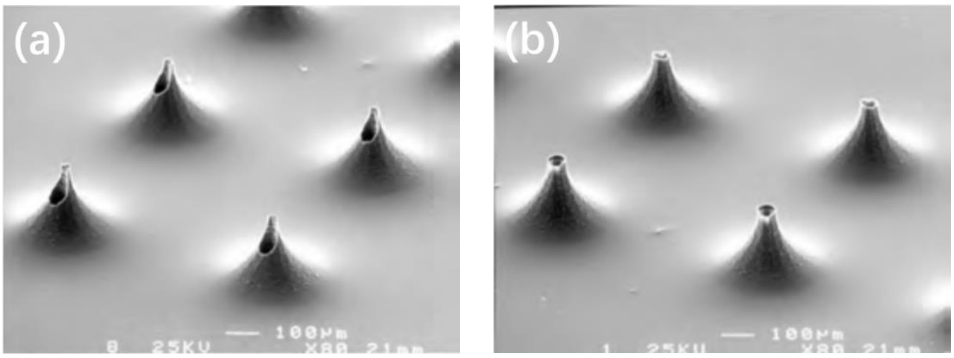

Figure 3.3 Hollow silicon microneedles by Stoeber and Liepmann[49]. The 200 μm long needles are fabricated by Bosch DRIE and sharpened by isotropic dry etching. (a) Pointed tip; (b) Flat tip.

Clogging issue must be considered discreetly once the microneedles were tested on human being no matter for drug delivery or biofluid extraction. In 2003, Griss and Stemme developed and demonstrated a concept of side-opened microneedles to realize a relatively low fluidic resistance. A three-dimensional needle structure was protruded in which the needle bore is located at the shaft of the needle as shown in Figure 3.4[50].

This side-opened design for drug delivery applications is being commercialized by Debiotech SA, Switzerland[47].

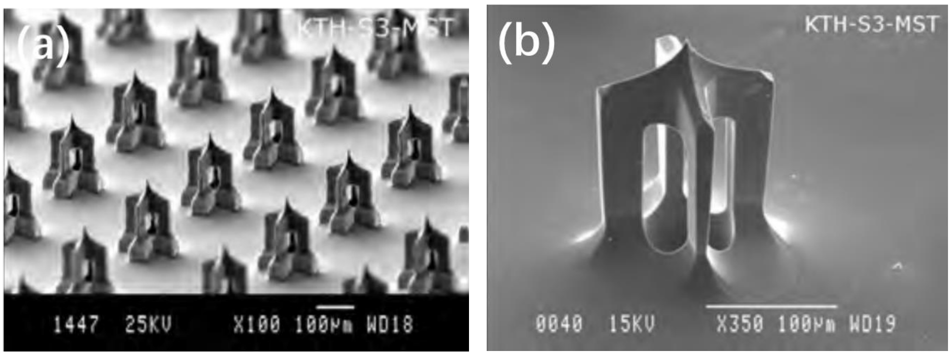

Figure 3.4 210 μm, cross-shaped, hollow, side-opened, silicon microneedles fabricated by Griss and Stemme. (a) Needles with a 50 μm long base shaft. (b) Needles without a base shaft[50].

This side-opened design was accepted by the academia and further developed by Roxhed et al. in 2005[51]. Compared to the previous design, the aspect ratio was increased in the new design by producing the silicon needles significantly longer to 400 μm as shown in Figure 3.5. In the meanwhile, the geometry of tips is changed from cross-shaped to circular to form a sharp and well-defined tip, thus the new design reveals superior penetration characteristics. In terms of all reported tests with this design, needles penetrated into skin using finger force without pretreatment of the insertion area[47].

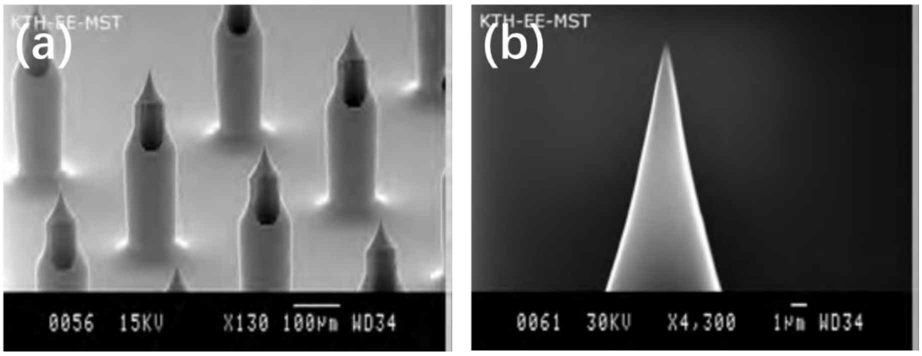

Figure 3.5 The circular side-opened design developed by Roxhed et al. (a) 400 μm long, ultra-sharp, side-opened microneedles. (b) Magnified view of the microneedle tip. The tip-radius is below 100 nm[51].

In 2003, wet etching approach was introduced in the fabrication process of silicon microneedles to sharpen the tip of needles resulting in intersecting crystal planes. Gardeniers' research group presented tetrahedrally-shaped hollow silicon microneedles by integrating DRIE and KOH etching techniques[52]. Figure 3.6 (a) shows a typical result of a 350 μm high microneedle with a triangular tip shape, a base of 250 μm, and a maximum hole width of 70 μm, and (b) presents a microneedle design with a round tip shape. In addition, this new alternative to fabricating sharp tip microneedles is being commercialized by NanoPass Ltd., Israel. The company also collaborated with GlaxoSmithKline on microneedle-based vaccine delivery and joint patents[53].

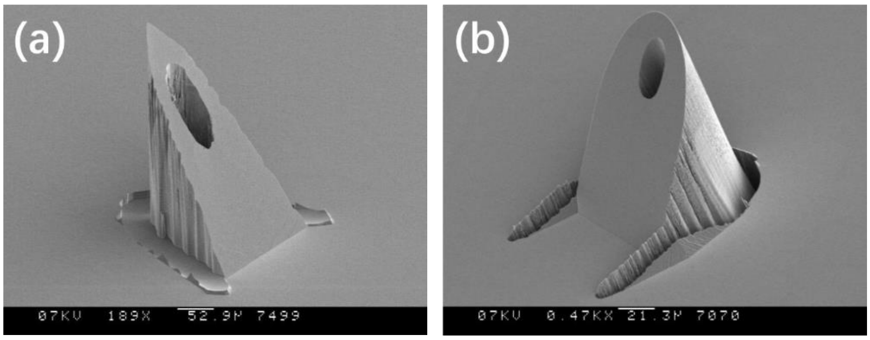

Figure 3.6 (a) SEM picture of a 350 μm high microneedle, with a base of 250 μm. (b) SEM picture of a microneedle with a tip with large radius of curvature[52].

3.3 Other materials for microneedle fabrication

As mentioned above, the microneedles are designed and fabricated in various shapes yet only based on silicon. In fact, the material choice should be more diverse due to high fabrication costs associated with silicon microneedles. Polymer and metal are two typical materials for microneedles fabrication.

3.3.1 Polymer microneedles

Polymer microneedles can be applied as a drug carrier with higher safety because of its biodegradable characteristics. In 2007, Jung-Hwan Park and his research group presented PDMS micromolding technique to fabricate an array of 200 PGA solid microneedles[54][55]. Microneedle master structures were fabricated using microlenses etched into a glass substrate that focused light through SU-8 negative resist to produce sharply tapered structures[55]. Figure 3.7 (a) shows the results after replicating SU-8 master structures using PDMS micromolding technique.

In the meantime, hollow out-of-plane polymer microneedle array design was realized by Sang Jun Moon and Seung S Lee using the LIGA (a German acronym for Lithographie, Galvanoformung, Abformung)) techniques with both vertical and inclined deep x-ray exposure[56]. Figure 3.7 (b) shows the fabricated hollow microneedle array based on PMMA.

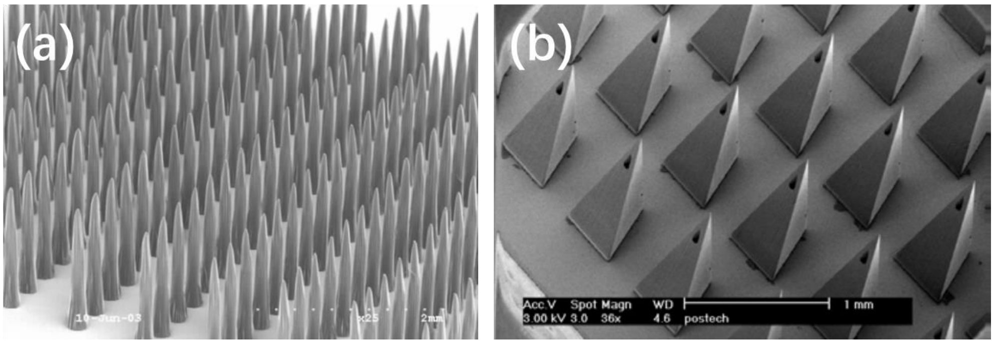

Figure 3.7 (a) SEM of tapered solid polymer microneedles. An array of 200 microneedles made of PGA biodegradable, in which each needle has a base diameter of 250 µm, a tip diameter of approximately 20 µm, and a length of 1500 µm[55]. (b) SEM image of the hollow PMMA microneedle array[56].

3.3.2 Metal microneedles

Besides polymer microneedles, metal is another ideal material especially for tall (e.g. up to 1 mm) microneedle fabrication because of its high mechanical strength, and established safety records in many medical applications[15][41][57].

In-plane hollow metal microneedles were first designed, fabricated and characterized by Brazzle, Papautsky et al. from University of Utah in 1998[58]. One year later, they modified the design from ‘multiple-needle’ to ‘single-needle with multiple output ports’[58][59] yet both fabricated in similar fashion. Figure 3.8 (a) shows the single-design with multiple ports published in 1999 which had 140 μm by 20 μm channel size, shaft dimensions of 200 μm by 60 μm, tip dimensions of less than 15 μm by 15 μm, a distance of 300 μm from tip to first outlet port and was 6 mm in length[15][59].

On the contrary, hollow out-of-plane metal needles were produced from SU-8 molds that were based on solid silicon microneedles[60]. Given the fact that the SU-8 layer can be cross-linked under UV light exposure, thin SU-8 layer was first spin-coated onto an array of solid microneedles. Then, the cross-linked SU-8 needle tips were exposed to plasma etching resulting in a hollow structure. In the following step, all the silicon was etched away by flipping over the samples. The final step was to sputter metal onto the SU-8 mold with conical holes to provide uniform surface to electroplate metal onto. Figure 3.8 (b) shows the hollow metal microneedles fabricated by the combination of lithography, RIE, and electroplating.

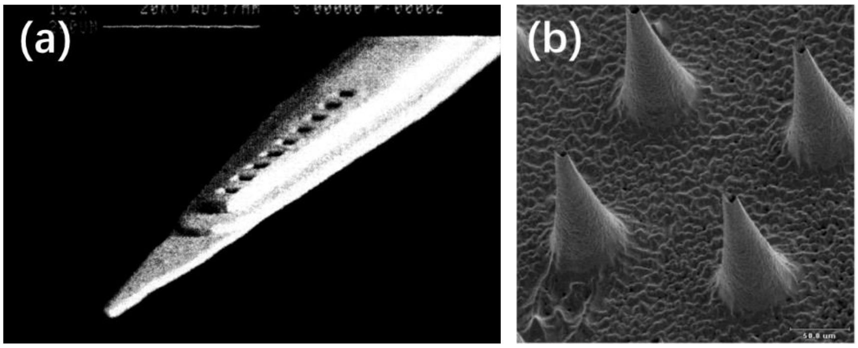

Figure 3.8 (a) SEM of hollow in-plane metal single-design microneedle. Shaft dimensions are 200 μm wide and 60 μm thick. Tip dimensions are less than 15 μm X 15 μm. Output ports are 30 μm^2[59]. (b) SEM of hollow out-of-plane metal (nickel-iron) microneedle array. It was arranged in a 20 by 20 array, 80 μm at their bases, taper to 10 μm at the tips, 150 μm in height, with 3 μm wall thickness and 150 μm center-to-center spacing[15][60].

3.4 Integrated microneedle devices

Over the past decades, integrated microneedle devices were created and developed to be functionalized as sensing unit. There are various types of integrated devices designed and fabricated in terms of diverse shapes of microneedles. Figure 3.9 shows a minimally-invasive self-calibrating glucose monitoring system designed by Zimmermann, Fienbork, et al[61]. Once the needle was filled with ISF, glucose diffused into dialysis fluid that passed an integrated flow-through enzyme-based glucose sensor[15][61].

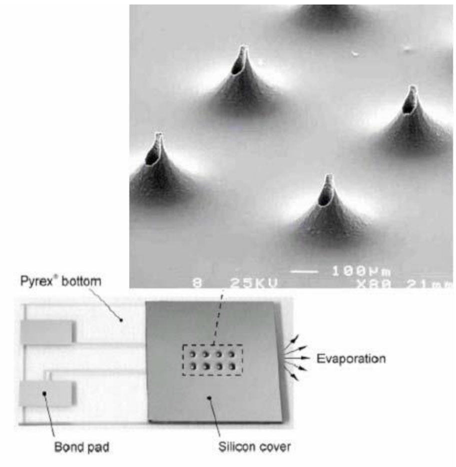

Figure 3.9 Prototype of microneedle-based glucose sensor that incorporates array of 8 hollow 200 μm tall silicon hollow microneedles, integrating with glucose sensor located in the Pyrex® fluidic channel underneath[61].

In 2004, an integrated fluidic system was designed by Mukerjee and his research group[17]. A reservoir for the fluid samples is connected to hollow microneedles on the backside of silicon wafer, by one or more micro-channels as shown in Figure 3.10. That ISF can be extracted into microchannels using only capillary action was claimed in Mukerjee’s paper.

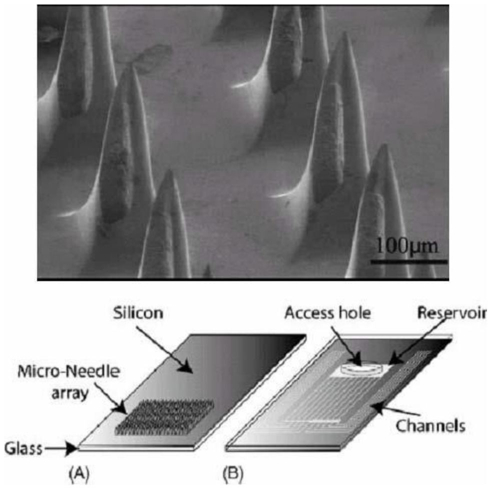

Figure 3.10 Schematics of (A) Front side (B) Backside of microneedles[17][15].

3.5 Conclusion

Extensive research has been performed in the microneedle field including both ex vivo and in vivo clinical trials. Advancements in microfabrication technology enables the realization of hollow microneedles, with the increasing interests in transdermal biological fluid extraction[62][17][63]. Even for the drug delivery, hollow microneedles are more desirable than solid microneedles for providing a better alternative in both the delivery quantity and more controllable flow rate. Such preferable transdermal systems require the high-level integration of microneedles and fluidic system.

This work aims at presenting an innovative double-side DRIE approach for producing hollow silicon microneedle arrays for skin penetration and transdermal skin fluid extraction.

Chapter 4 Methods

This chapter describes the method developed to fabricate hollow silicon microneedle arrays including key techniques such as lithography, DRIE, and wet etching. An innovative double-side DRIE approach is also presented in detail. Skin penetration and ISF extraction were applied on human's skin for in vivo tests.

4.1 Chip design

The goal of the process is to make a hollow silicon needle-shape array for ISF extraction in an innovative double-side DRIE approach. The basic logic behind our process is as follow: define the bore-hole structure on one side of wafer then pillar structure on the other side; afterward, sharpen the pillars into needles while exposing the bore-holes at the same time. Therefore, our process includes three essential steps: lithography, DRIE and wet etching. The backgrounds of these techniques have been introduced in Chapter 2.

Three different designs for the microneedle tip shape were investigated based on Mukerjee's paper termed as 'volcano-like', 'micro-hypodermic' and 'snake-fang' design[17]. The only difference between them is the relative position of the central bore hole to the shaft of the needle. Figure 4.1 shows three different fashions designed by Mukerjee. In 'volcano-like' design, the silicon walls at the tip are relatively fragile and the centered bore will be blocked with tissue that will prevent ISF extraction. Compared to ‘volcano-like’ design, ‘micro-hypodermic’ design proved robust microneedles to penetrate skin without any breakage. However, this design also exhibited bore hole plugging problems. Therefore, based on the ‘snake-fang’ fashion, our microneedle array was designed as shown in Figure 4.2. Peripheral supporting solid needles can enhance the penetration. The bore holes were shifted 30 μm from the center of the column.

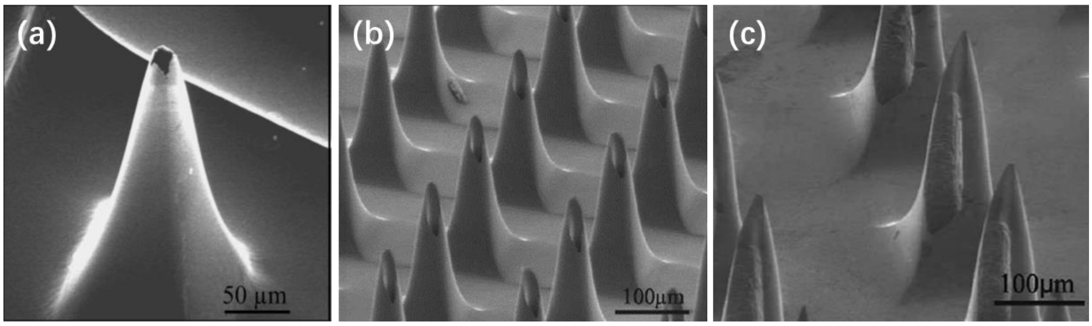

Figure 4.1 SEM pictures of three different designs (a) ‘volcano-like’, (b) ‘micro-hypodermic’, and (c) ‘snake-fang’[17].

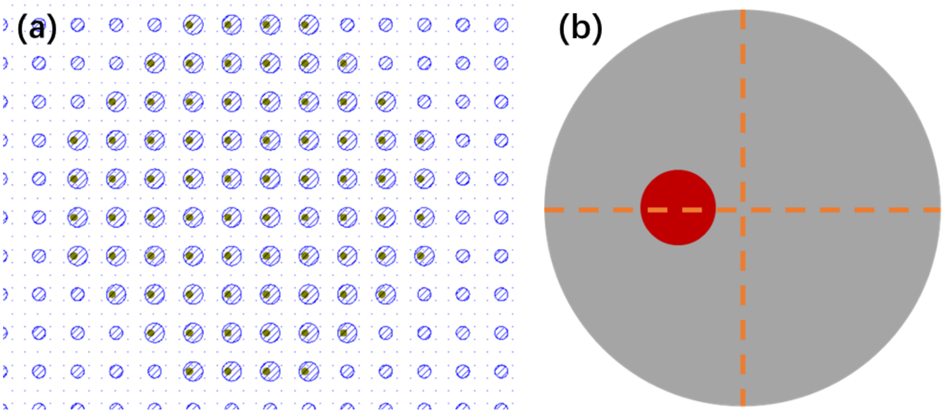

Figure 4.2 The design of hollow microneedle array. (a) 200 μm in diameter pillars and 40 μm in diameter holes with 76 holes per die. (b) 30 μm offset from the central bore hole to the center of the pillar.

4.2 Fabrication process

The proposed fabrication process for hollow silicon microneedles is demonstrated in Figure 4.3. First, a single layer of AZ 4620 photoresist at a thickness about 10 μm was spun onto one side (termed as the ‘backside’) of a 4-inch wafer (double-side polished, Fig 4.3a). Standard photolithography was then applied to pattern this photoresist, forming holes that are approximately 30 μm in diameter (Fig 4.3b). DRIE (i.e. the Bosch process) was performed to etch bore holes 300 μm deep into the backside of the wafer defining a high aspect ratio structure (around 1:10 HAR, Fig 4.3c). Note that at this moment the other side of the wafer (termed as ‘frontside’) is still flat. The DRIE process was halted before the bore-holes were etched through the wafer to its frontside. Similar to the backside patterning, the frontside pillar pattern was defined (Fig 4.3d) with the double-sided alignment to the holes on the backside. The AZ 4620 photoresist was patterned to create cylindrical pillars aligned to the bore-holes. This alignment also enabled accurate patterning of holes such that their centers were offset with the circles that defined needle. This was to address tissue coring within the needle bore during insertion[17]. Pillars of approximately 300 μm in height and 200 μm in diameter were then etched by DRIE (Fig 4.3e), making an overlap of 100 μm between the pillars and holes. At this point, the bore-holes were still not exposed on the frontside; essentially they are still buried channels. Afterward, using a mixed solution of hydrofluoric acid and nitric acid, the circular pillars were sharpened into needles and the through wafer holes were fully opened (Fig 4.3f and 4.3g). This was possible by taking advantage of the isotropic etching nature of the chemical mixture, i.e., the etching rate decreases from the needle tip to the base[32]. Holes were exposed on the side wall of the needles creating channels from the needles to the wafer's backside. This final step is a critical and novel process for creating hollow microneedle structures.

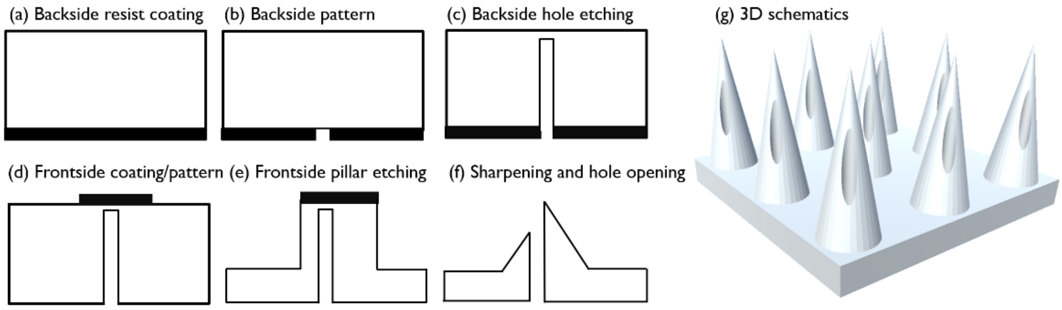

Figure 4.3 Schematic fabrication processing of hollow silicon microneedle arrays. (a) Spin coating on the backside, (b) Standard lithography, (c) DRIE on the backside, (d) Backside alignment lithography, (e) DRIE on the frontside, (f) Wet etch.

4.2.1 Photolithography

Standard cleaning procedures for silicon wafers were established before performing lithography. Silicon wafers are cleaned by an HF dip and DI rinse, followed by acetone and isopropanol (IPA) rinsing and blowing dry with a N_2 gun. To remove residue on the surface of a wafer prior to processing, oxygen plasma treatment can be also applied to the wafers afterwards. A following dehydration bake is necessary to remove all moisture from the surface of the wafer. The silicon wafer is placed face up on the hot plate in soft contact at 120°C for 3 minutes. After cooling to room temperature, the next step is to spin coat one layer of hexamethyldisilazane (HMDS) which serves as an adhesion promoter for the photoresist application. HMDS is spin coated at 3000 rpm for 30 seconds and dries completely after the spin coating. The whole process requires 30 minutes to complete.

Positive photoresist AZ 4620 with a thickness about 10 μm was spun onto the backside of a double-side polished wafer at 2000 rpm for 40 seconds followed by standard photolithography. Figure 4.4 (a) (b) shows the hole and pillar pattern after lithography with HMDS coating prior to photoresist application, and (c) presents a poor result caused by spin coating photoresist without HMDS treatment.

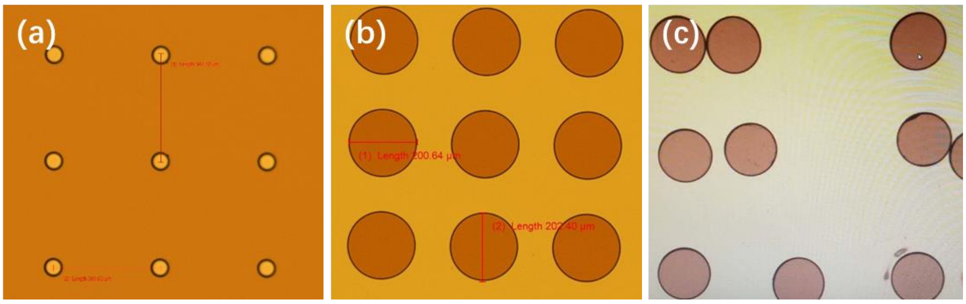

Figure 4.4 The pattern is defined after standard lithography and development with and without HMDS coating. HMDS promotes the adhesion to define a better pattern. Otherwise, structures migrate on the wafer. (a) 30 μm in diameter holes, 300 μm pitch. (b) 200 μm diameter pillars. (c) Structures migrating after photoresist development.

In the process of pillar side lithography, various diameters of pillars have been designed as shown in Figure 4.5. Pillars surrounded by a ring structure were introduced into the design to protect the pillars from undercut during DRIE.

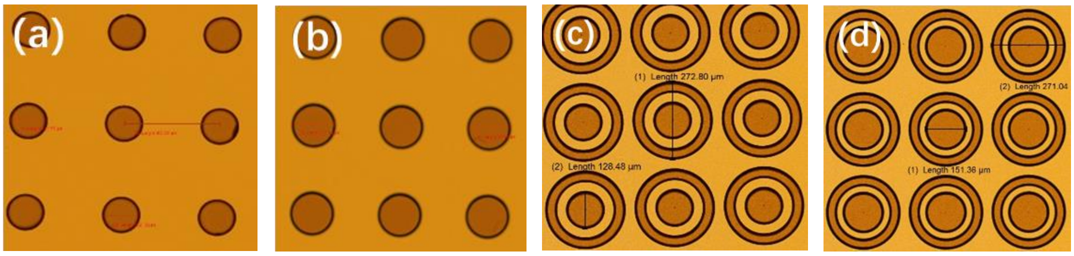

Figure 4.5 (a) 100 μm in diameter pillars. (b) 150 μm in diameter pillars. (c) 130 μm ID 270 μm OD. (d) 150 μm ID 270 μm OD.

Furthermore, backside alignment is a key step to precisely placing the holes with different offsets relative to the center of the pillars. Figure 4.6 shows the alignment process in detail. The picture of mask aligner is taken before loading the sample as shown in Figure 4.6 (a), and then aligning the marks accurately is shown in Figure 4.6 (b).

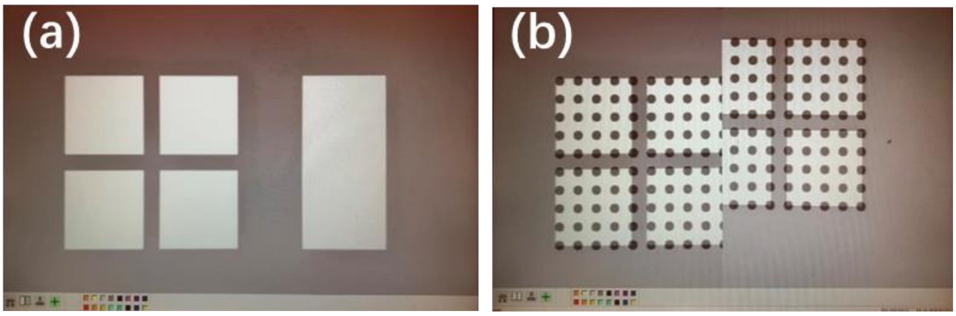

Figure 4.6 Backside alignment process in Karl SUSS MA6. (a) Capture the pattern on the mask only. (b) Align the marks accurately by rotating X, Y, Z knobs.

A series of experiments has been carried out on the backside alignment lithography. After 600 cycles of Bosch process DRIE to define pillars, holes will be exposed if a large misalignment exists between them. Otherwise, holes will be set precisely inside the pillars to create the approximate 100 μm overlap. Figure 4.7 shows the results of both well-established alignment and misalignment after running a DRIE process.

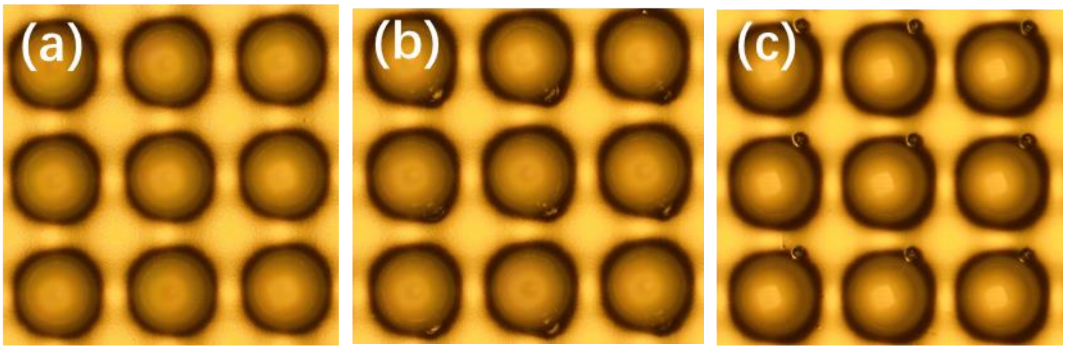

Figure 4.7 The results of both well-established alignment and misalignment after DRIE process in the microscope. (a) well aligned, (b) less than 50 μm misalignment, (c) more than 50 μm misalignment.

4.2.2 DRIE

Cryogenic and Bosch-based DRIE can be considered as two main technologies for high-rate DRIE, although the Bosch process is the only recognized production method[64]. The essential issues with cryo-DRIE is that photoresist or other masks crack under extreme cold condition, and the by-products have a tendency of depositing on the nearest cold surface such as the substrate and electrode [64][65][66]. For many applications of DRIE, the main goals are usually in producing trenches or other features of very high aspect ratio[67].

In our case, the standard Bosch process recipe developed at the Quantum NanoFab at University of Waterloo has been applied for both our pillar and hole etching to achieve a high aspect ratio feature. The etch rate is around 400 nm/cycle (each cycle 12 seconds) and uniformity is approximately 2%. Our target is to obtain ~350 μm deep holes 30 μm in diameter and pillars approximately 300 μm high and 100 μm in diameter.

In the preliminary experiments, 300 cycles Bosch processing was exploited to produce 110 μm deep holes with a vertical profile, but the diameter was enlarged from 30 μm to 50 μm. Figure 4.8 (a) shows the cross-section view after 300 cycles of Bosch processing and (b) gives a clear clue about the diameter change after DRIE.

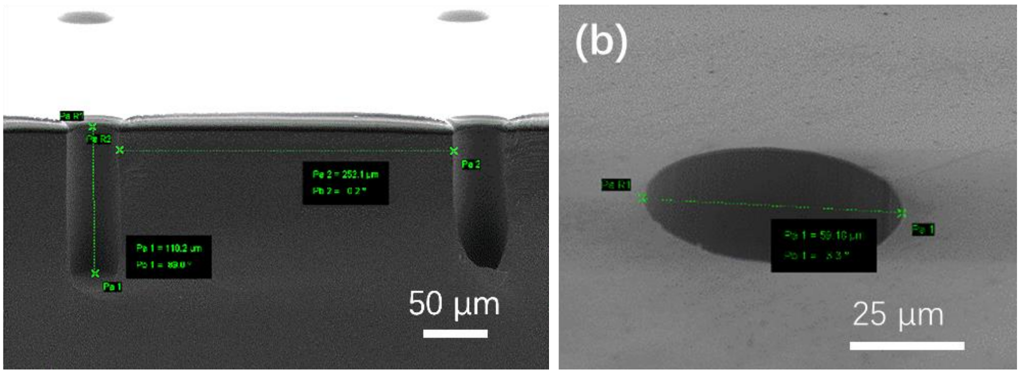

Figure 4.8 SEM results after 300 cycles of Bosch processing. (a) A cross-section view. (b) A 70°top view.

Subsequently, 1500 additional cycles were added on the samples above. Approximately 6 more hours of DRIE processing generated the holes to a depth of 400 μm. It was observed that a significant overcut was present and that the diameter was enlarged to 126 μm. Figure 4.9 shows the results after the total 1800 cycles.

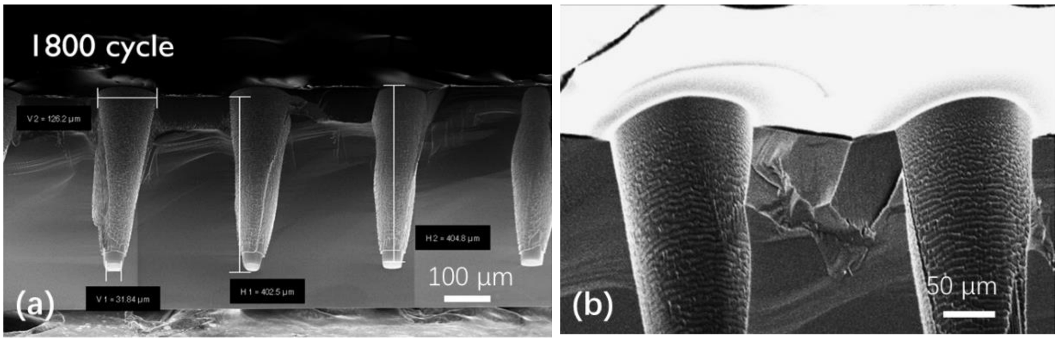

Figure 4.9 The SEM picture after 1800 cycles of Bosch processing. (a) A cross-section view. (b) A zoomed-in view.

As shown in Figure 4.9, the diameter and profile should be more effectively controlled to form vertically deep holes 30 μm in diameter. Aspect ratio dependent etching (ARDE) is widely reported for deep silicon etching. Figure 4.10 (a) shows an example of ARDE of trenches in varying widths. Figure 4.10 (b) illustrates the ARDE lag measured as trench depths are normalized to that of a 100-μm-wide trench[68].

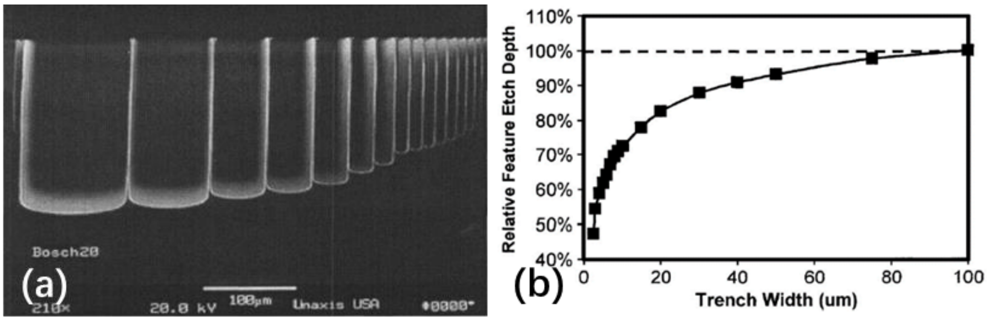

Figure 4.10 (a) ARDE lag exhibited in typical TDM plasma etch process. The final etch depths in wider trenches are larger. (b) A plot of trench depth normalized to that of a 100-μm-wide trench. An ~50% ARDE lag is observed in a 2.5-μm-wide trench[68].

The etch rate rapidly decreases with the aspect ratio; over a certain critical point of aspect ratio, the etch rate likely reaches a constant minimal value, all while the etch mask is constantly consumed therefore resulting in lateral etching on the surface. Thus, both enhancement of photoresist selectivity and optimization of the etching recipe are required to mitigate the consequences of ARDE.

For etching deeper holes with a vertically straight profile, the depassivation time and bias voltage should be respectively increased to remove the passivation polymer at the bottom of the holes by enhancing the ion bombardment.

The DRIE machine at University of Toronto, which offers a high selectivity of up to 1:200, was used to optimize the recipe. Figure 4.11 (a) shows the SEM results after etching with different optimized recipes. By ramping the process pressure, increasing the RF power, and adjusting the length of Argon bombardment time, we are able to produce holes approximately 310 μm deep and 30 μm in diameter as shown in Figure 4.11 (b); (c) gives a top view of the holes after DRIE. The diameter remained at 30 μm. Therefore, holes ~310 μm deep and 30 μm in diameter can be achieved by an optimized recipe, consisting of increased RF power followed by a high aspect ratio etching recipe. The whole DRIE process is only 1 hour in duration which is comparatively a low cost and time efficient solution.

A 3D optical profilometer was used to measure the surface roughness as shown in Figure 4.12. The mean roughness was found to be around 400 nm and the root mean square roughness about 500 nm.

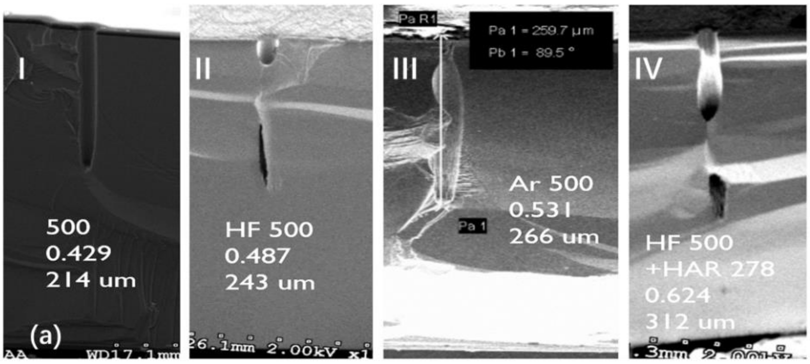

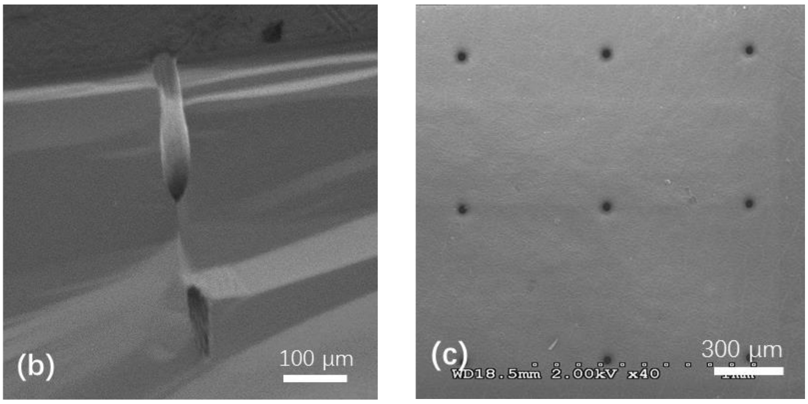

Figure 4.11 (a) From left to right, SEM results are shown after 500 cycles etching with each recipe. I. shows the result with an original recipe. A 214 µm deep hole with a critically vertical profile. II. By modifying the RF power from 100W to 120W, 243 µm deep holes can be fabricated. III. By modifying Ar time from 700 ms to 800 ms, deeper holes with a 266 µm depth can be defined. IV. The best recipe is 500 cycles with 120W power optimized recipe followed by a high aspect ratio recipe for 278 cycles. (b) A zoomed-in view of the hole. (c) A top view of the holes.

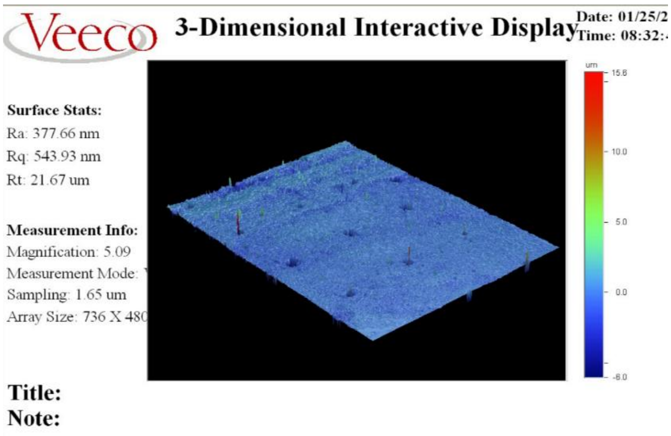
3-Dimensional Interactive Display

Date: 01/25/2
Time: 08:32:

Surface Stats:
Ra: 377.66 nm
Rq: 543.93 nm
Rt: 21.67 um

Measurement Info:
Magnification: 5.09
Measurement Mode:
Sampling: 1.65 um
Array Size: 736 X 480

Title:
Note:

Figure 4.12 The characterization of surface roughness on the backside of silicon.

On the other side, DRIE on the frontside of the wafer is more reliable; fabricating pillars ~330 µm tall 200 µm in diameter was possible due to a low aspect ratio dependency. At the beginning, 300 and 900 cycles of the Bosch process were applied separately on the pillars to test the profiles. Figure 4.13 shows the pillar profiles after (a) 300 cycles (b) 900 cycles etching. The pitch was 300 µm for both samples while the diameters varied from 100 µm and 150 µm respectively.

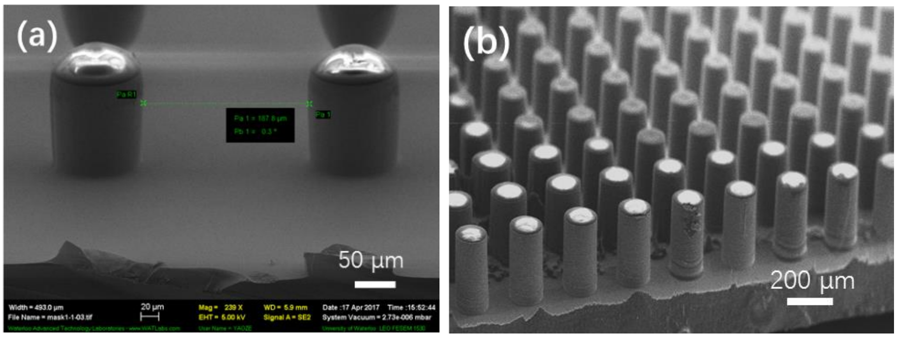

Figure 4.13 SEM pictures after Bosch process etching. (a) 300 cycles. The pillar is ~100 µm tall and 100 µm in diameter. (b) 900 cycles. The pillar is ~330 µm tall and 150 µm in diameter.

In the following experiments, the combination of holes and pillars is the key step to defining hollow structures. As mentioned in Figure 4.7, the perfect well-aligned structure is formed on the backside via alignment lithography. Figure 4.14 shows the integration of holes and pillars after double-sided etching; (a) misalignment (b) well-aligned. Figure 4.15 shows another design where solid pillars are positioned between hollow pillars to enhance chip robustness and strength when the pillars are subsequently sharpened into needles and inserted into skin.

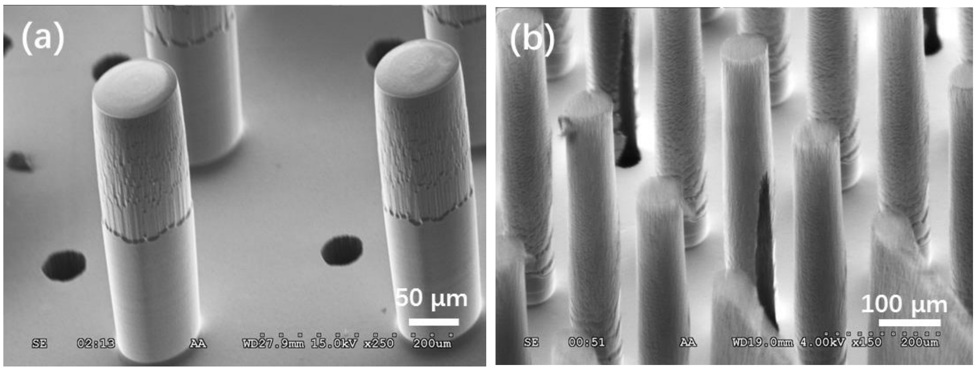

(a) (b)

Figure 4.14 The integration of holes and pillars. (a) misalignment between pillars ~80 µm in diameter and holes 40 µm in diameter; (b) pillars well-aligned to bore holes. After DRIE, bore holes are exposed at the base of columns.

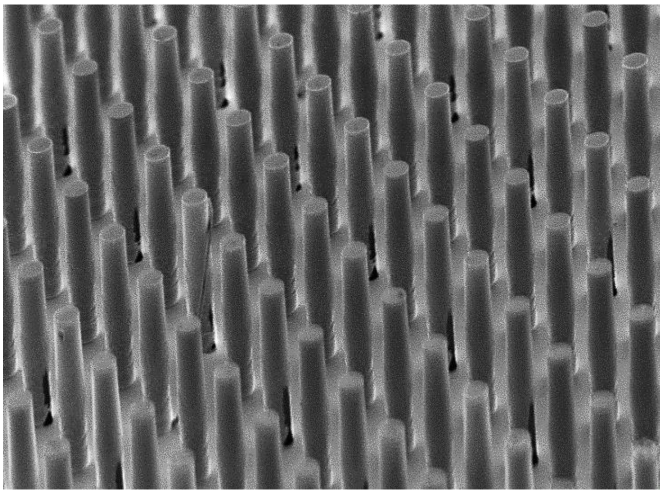

Figure 4.15 An array of pillars with a hollow structure. The center to center spacing is 300 μm. In this design, 50% of the needles have bored holes for ISF collection, and the other half are solid to distribute the pressure.

4.2.3 Wet etching

As discussed in the Chapter 2, a static wet etching system consisting of a solution of HF (49%)–HNO_3 (69%) mixed at a ratio of 1:19 by volume was set up in this work to sharpen silicon pillars into a sharp needle-shaped profile.

In the preliminary experiments, solid pillars were used to perform wet etching tests to obtain solid needles. Figure 4.16 shows pillars 200 μm high and 100 μm in diameter after acetone, IPA, photoresist stripper and oxygen plasma treatments were performed to remove photoresist on their tops.

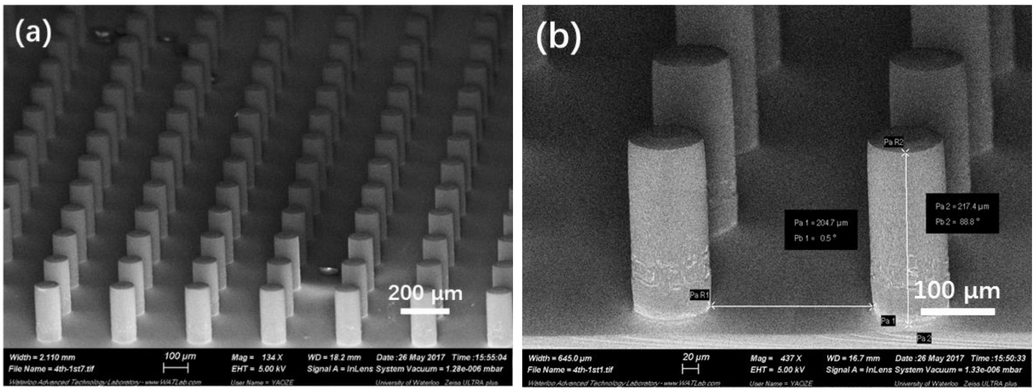

Figure 4.16 The SEM results of pillars after DRIE process, 200 µm high and 100 µm in diameter. (a) Solid pillar array. (b) A zoomed-in view of pillars.

Figure 4.17 shows the SEM results after 20 mins of wet etching. The tip diameter is approximately 60 µm while the base was measured to be approximately 90 µm in diameter. The height of the pillars is approximately 190 µm. From this result, we concluded that the vertical shrinkage is much less than the lateral tip shrinkage while the etching rate decreases gradually from the needle tip to the base.

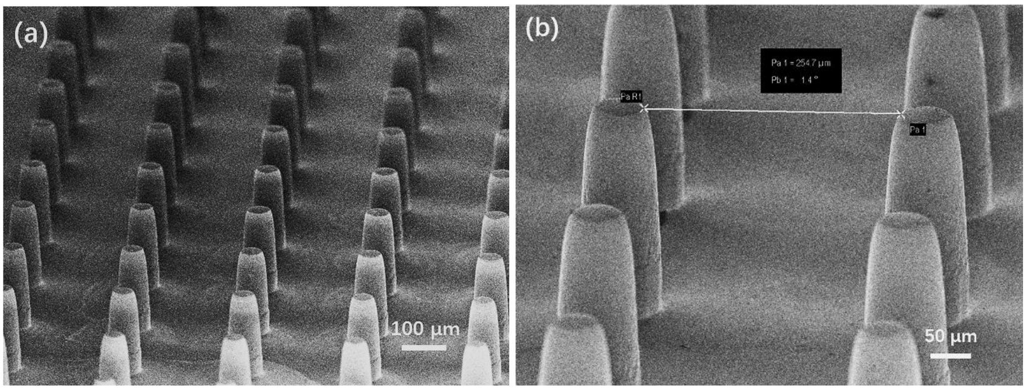

Figure 4.17 SEM pictures demonstrate the blunt cone-shaped pillars. (a) high uniformity of the wet etch; (b) a zoomed-in view.

Another 20 mins of wet etching was performed subsequently. Figure 4.18 presents a very sharp solid microneedle array. The pillar height decreased from 200 µm to 150 µm, and simultaneously the diameter at the base decreased from 100 µm to 70 µm while the tip radius decreased dramatically to less than 5 µm.

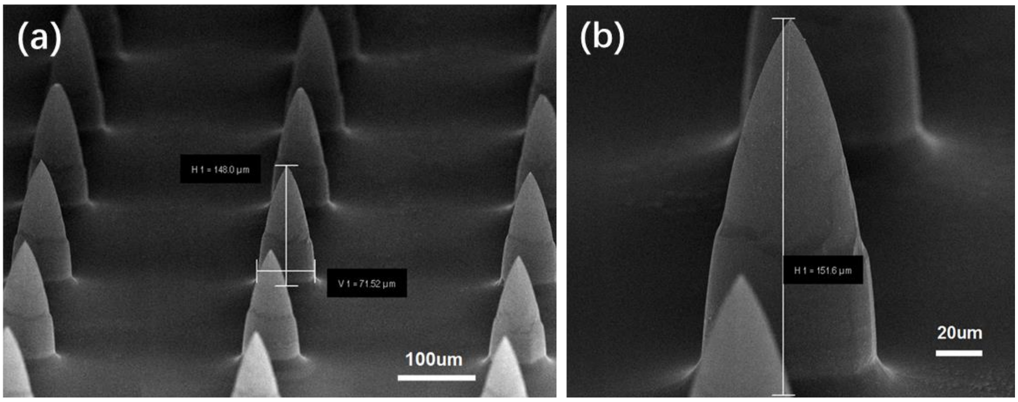

Figure 4.18 SEM image shows (a) high uniformity of a solid silicon microneedles array, and (b) the zoomed-in view of an individual sharp needle.

Over-etching will be present for statically etching for an excessive amount of time or dynamic etching. Figure 4.19 shows two types of over-etching caused by employing excessive static and dynamic etching times respectively. The height of needles decreased to approximately 20 μm or in some cases less than 10 μm.

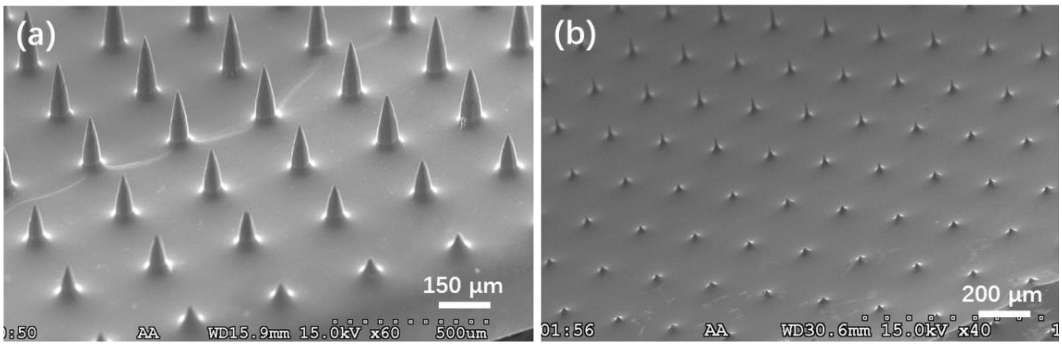

Figure 4.19 SEM image showing the shape of over-etching due to (a) 60 min of static etching; (b) 10 min of dynamic etching.

After successfully producing sharp solid microneedle array, combining holes with needles to create the hollow structure was the next step. Various hollow shapes can be achieved by placing bore holes with different offsets relative to the center of the pillars. In our experiments, ‘micro-hypodermic’ and ‘snake-fang’ fashions were produced as Figure 4.20 shows.

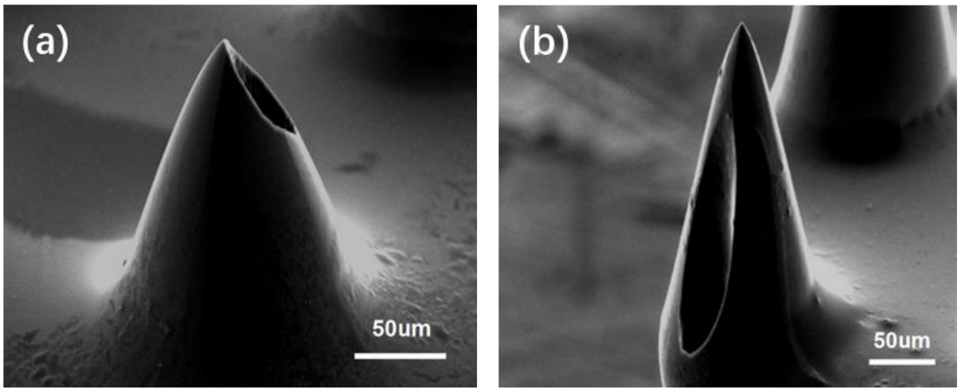

Figure 4.20 SEM image showing the hollow Si microneedles with two different hole offsets for producing (a) the ‘micro-hypodermic’, and (b) ‘snake-fang’ fashions of microneedle design.

Although the bore hole in the ‘micro-hypodermic’ needle design is elongated along the side of the needle, the potential of coring skin during ISF extraction may be present[17]. Thus, the ‘snake-fang’ design was fabricated in form of an array. Figure 4.21 (a)-(d) shows the ‘snake-fang’ hollow silicon microneedle array with different needle base diameters; (e) and (f) demonstrate a solid-hollow microneedle array and a needle height of approximately 300 μm, larger than that of Figure 4.21 (a)-(d).

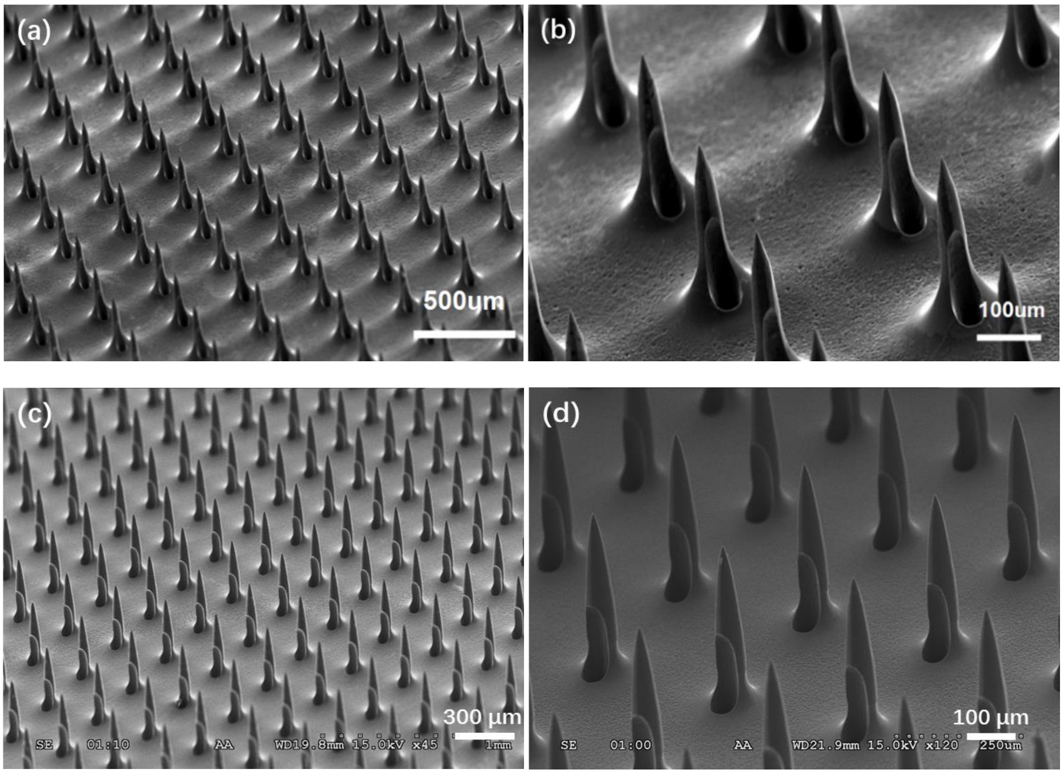

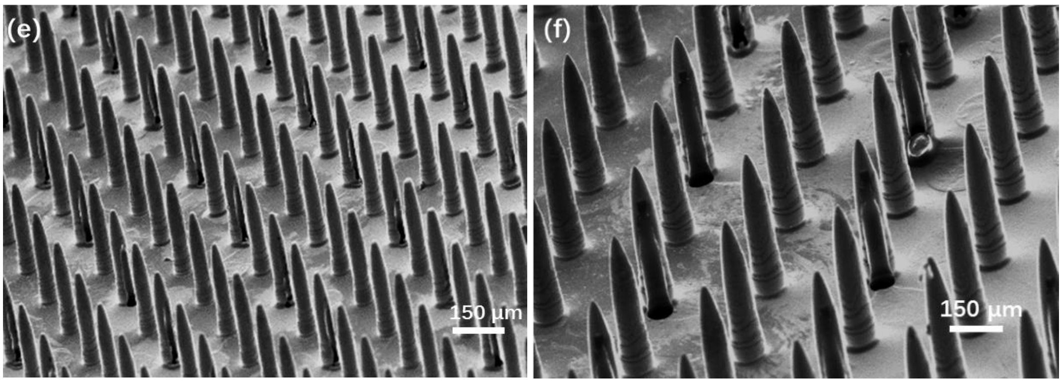

Figure 4.21 SEM images showing: (a)-(d) the hollow silicon microneedle arrays with different needle base diameters: (a) 200 µm high and 100 µm in diameter at the base; (b) a zoom-in view of (a); (c) 200 µm high and 60 µm in diameter at the base; (d) a zoom-in view of (c); (e)-(f) a solid-hollow composite silicon microneedle array: (e) 50% of the needles have bored holes for ISF collection, and the other half are solid to distribute the pressure during skin insertion; (f) a zoomed-in view of microneedles 300 µm high and 80 µm in diameter.

4.3 In vivo tests

Confirmation of the above fabricated microneedle arrays piercing skin was achieved by dye penetrant inspection (DPI). Pig skin was penetrated first for the preliminary tests in this work. Figure 4.22 (a) shows the evidence of friction adhesion between the array and human skin after skin penetration as shown in Mukerjee's paper[17]; (b) shows a successful penetration test on the pig skin in our work. By holding the microneedle array with a tweezer, the pig skin can be moved upwards due to the friction adhesion; (c) presents a clear pattern on the pig skin which can be observed by the naked eyes.

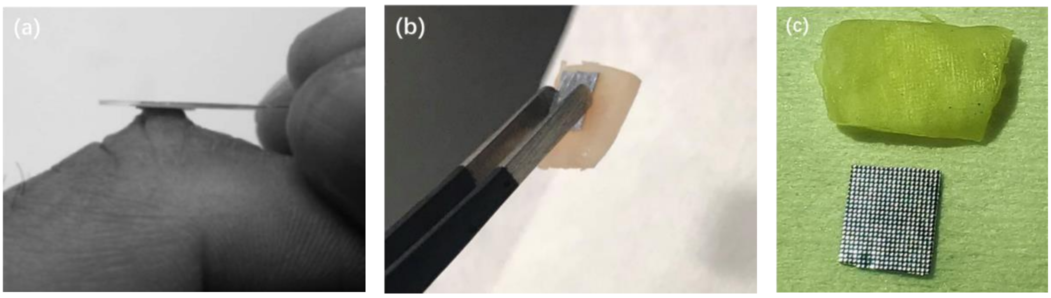

Figure 4.22 (a) Friction adhesion between the microneedle array and the skin surface as shown in Mukerjee's paper[17]. (b) A successful penetration test on the pig skin in our work. (c) The appearance of the needle pattern on pig skin.

A set of hollow microneedle arrays were applied onto human skin in the following experiments. The earlobe was selected as a penetration site since it is less elastic than other skin areas and allows pressure to be applied on both sides of the array. The earlobe was first cleaned with IPA and then pierced by the hollow microneedle array. Afterwards, Methylene Blue was placed on the skin and subsequently wiped away after 1 min. Figure 4.23 (a) reveals that Methylene Blue migrated down through the highly impermeable stratum corneum that was breached by the microneedle arrays. Figure 4.23 (b) shows that the majority of needles stand well after penetration likely due to the force distribution among all the needles in the array.

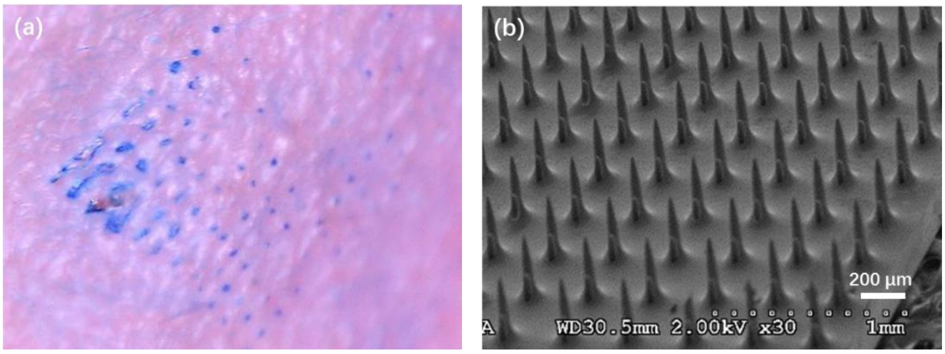

Figure 4.23 (a) Methylene Blue used on the insertion site and was later imaged on the earlobe to demonstrate a successful penetration. (b) an SEM image of the microneedle array after insertion.

Ongoing work will focus on ISF extraction by using an integrated system consisting of a microneedle arrays and reservoirs. Figure 4.24 shows the assembly of a microneedle array and a reservoir system. PDMS was cut out into desired dimensions with a reservoir facing the backside of the microneedle array. By using oxygen plasma cleaning and heating assembly on hotplate, the PDMS reservoir was bonded to the silicon microneedle array as shown in Figure 4.24 (a). About 80 cm of PTFE tubing was inserted into PDMS to connect the reservoir to a syringe pump as shown in Figure 4.24 (b).

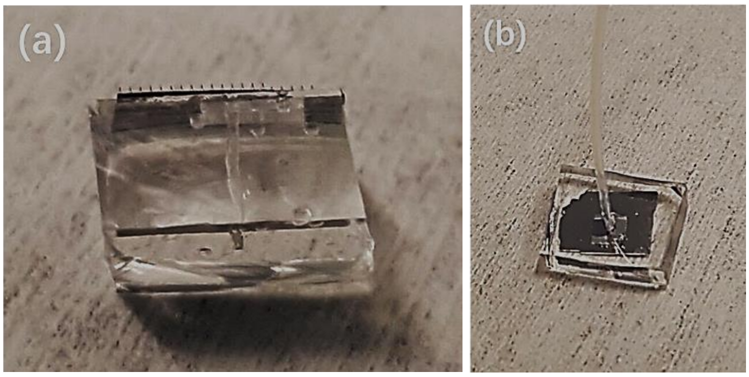

Figure 4.24 The prototype of the assembled extraction apparatus. (a) A side view of the extraction device without the PTFE tubing. (b) A top view of the microneedle-reservoir system.

Extraction tests with this microneedle-reservoir system were performed on a human arm using the following procedure. Insert the microneedles into skin by pushing on the device with thumb pressure on center of the array and then holding the device in place for about 20 min. Immediately afterwards, set syringe pump to withdraw fluid at predetermined fluid extraction rate for a predetermined total volume. Once the withdrawal process is complete, detach microneedle array from skin by lifting directly outwards. The sample was then baked at 150° C for 2 hours to keep the residual organic material. Figure 4.25 shows SEM results of the microneedle array before and after extraction tests.

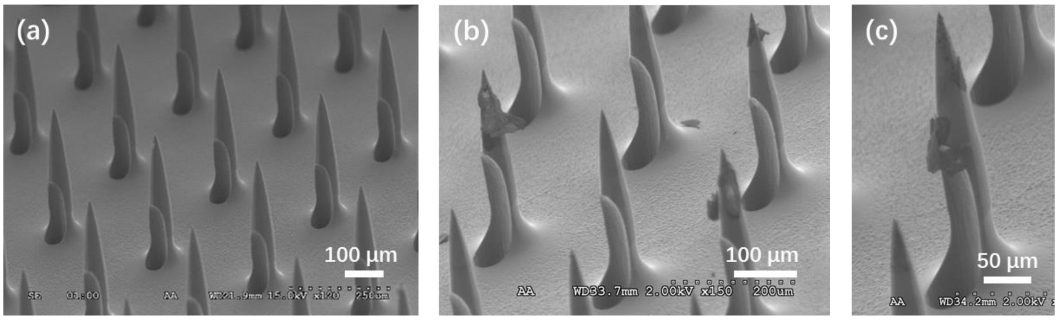

Figure 4.25 (a) An SEM image of the microneedle array before insertion. (b) and (c) The tissue and liquid residual remained on the needle.

These exciting results presented above can prove that the hollow silicon microneedle array can penetrate through the highly impermeable outer-most layer of skin and reach the epidermis layer in which ISF is located. ISF was extracted successfully inside the bore hole of the microneedles. In the future, the microneedle-reservoir apparatus will be optimized and ISF extraction by the capillary force will also be concentrated on.

Chapter 5 Conclusion

The fabrication of hollow silicon microneedle array and in vivo testing of a microneedle-reservoir integrated assemble system are presented in this thesis.

This work illustrates an innovative double-side DRIE approach for producing hollow silicon microneedle arrays. In the experiments, solid microneedles with tip radii less than 5 μm were fabricated by performing DRIE and the subsequently wet etching on the frontside only. Afterwards the etching from both sides were integrated, resulting in the accomplishment of the hollow Si microneedles with two bore placements. Hollow silicon microneedle arrays with 200 μm and 300 μm in height were fabricated successfully as well. Such microneedles can only penetrate through the outer layer of skin without interfering with the nerve endings in the deeper layer, making minimal invasive and painless sampling fashion.

All the promising results from the fabrication and in vivo testing confirm that hollow silicon microneedle arrays are not only sharp enough to penetrate the stratum corneum but also robust enough to extract ISF out of skin. Ongoing work will focus on the optimization of the assemble extraction apparatus and the capillary filling of the holes.

Reference

[1] N. Olsman and L. Goentoro, “There’s (still) plenty of room at the bottom,” *Current Opinion in Biotechnology*, vol. 54. pp. 72–79, 2018.

[2] C. R. K. Marrian and D. M. Tennant, “Nanofabrication,” *J. Vac. Sci. Technol. A Vacuum, Surfaces, Film.*, vol. 21, no. 5, pp. S207–S215, 2003.

[3] A. H. Tatau Nishinaga, Yasushiro Nishioka, Hiroshi Ito, “Proceedings of the Third International Symposium on the Control of Semiconductor Interfaces,” *Appl. Surf. Sci.*, p. Xiii, 2000.

[4] J. Zhang, “Nanofabrication and its application in plasmonic chemical and bio-sensors,” University of Waterloo, 2014.

[5] C. Combs and M. Nichols, “Introduction To Micro/Nano Fabrication,” *Life Sci.*, vol. 91, no. 23–24, p. 1140, 2012.

[6] D. Mijatovic, J. C. T. Eijkel, and A. van den Berg, “Technologies for nanofluidic systems: top-down vs. bottom-up—a review,” *Lab Chip*, vol. 5, no. 5, p. 492, 2005.

[7] V. Coaters, “PHYSICAL VAPOR DEPOSITION (PVD) PROCESSES by Donald M . Mattox I----1,” *Vacuum*.

[8] V. Sunil and K. Channam, “Synthesis of strongly correlated oxides and investigation of their electrical and optical properties,” 2017.

[9] WIKIBOOKS, “Nanotechnology/Top-down and bottom-up approaches.” [Online]. Available: https://en.wikibooks.org/wiki/Nanotechnology/Top-down_and_bottom-up_approaches.

[10] S.D.Senturia, *Microsystem Design*. Springer, 2005.

[11] M.J.Madou, *Fundamentals of Microfabrication and Nanotechnology*, 3rd ed. CRC Press, 2011.

[12] N.Maluf, *An Introduction to Microelectromechanical Systems Engineering*, 2nd ed. Artech House, 2000.

[13] D. R. Ramadoss, “MEMS devices for biomedical applications,” *SolidStateTechnology*.

[14] SENSIMED, “Sensimed’s TriggerfishTM implantable MEMS IOP sensor.” [Online]. Available: http://www.sensimed.ch/en/.

[15] W. Martanto, “Microinjection into skin using microneedles,” 2005.

[16] WIKIPEDIA, “Human skin.” [Online]. Available: https://en.wikipedia.org/wiki/Human_skin.

[17] E. V. Mukerjee, S. D. Collins, R. R. Isseroff, and R. L. Smith, “Microneedle array for transdermal biological fluid extraction and in situ analysis,” *Sensors Actuators, A Phys.*, vol. 114, no. 2–3, pp. 267–275, 2004.

[18] G. Schmidt, Robert F., Thews, *Human Physiology*, 2nd ed. 1989.

[19] WIKIMEDIACOMMONS, “Structure of the skin,” 2013. [Online]. Available: https://commons.wikimedia.org/wiki/File:501_Structure_of_the_skin.jpg.

[20] G. Tortora, *Principles of anatomy and physiology*, 5th ed. New York, 1987.

[21] P. C. Benias *et al.*, “Structure and Distribution of an Unrecognized Interstitium in Human Tissues,” *Sci. Rep.*, vol. 8, no. 1, p. 4947, 2018.

[22] M. E. Circuits, J. S. Kilby, and E. a Suominen, “U.S. Patent 3,138,743,” 1964.

[23] R. N. Noyce, “Semiconductor device-and-lead-structure,” 1961.

[24] F. M. Li, “Organic Thin Film Transistor Integration by,” University of Waterloo, 2008.

[25] Nanosystem Fabrication Facility, “Wet and Dry Etching Table,” 2014. [Online]. Available: http://www.nff.ust.hk/en/equipment-and-process/process/wetdryetchingtable.html.

[26] Wikipedia, “Etching (microfabrication),” 2018. [Online]. Available: https://en.wikipedia.org/wiki/Etching_(microfabrication).

[27] M. Östling, “Etching: Requirements at the Nanoscale,” Stockholm, 2013.

[28] Y. Chen and A. Pépin, “Nanofabrication: Conventional and nonconventional methods,” *Electrophoresis*, vol. 22, no. 2, pp. 187–207, 2001.

[29] M.-K. L. Simon M. Sze, *Semiconductor Devices: Physics and Technology*. 2012.

[30] N. Wilke, A. Mulcahy, S. R. Ye, and A. Morrissey, “Process optimization and characterization of silicon microneedles fabricated by wet etch technology,” *Microelectronics J.*, vol. 36, no. 7, pp. 650–656, 2005.

[31] H. Robbins and B. Schwartz, “Chemical etching of silicon I,” *J. Electrochem. Soc.*, vol. 106, no. 6, pp. 505–508, 1959.

[32] R. Bhandari, S. Negi, L. Rieth, and F. Solzbacher, “A wafer-scale etching technique for high aspect ratio implantable MEMS structures,” *Sensors Actuators, A Phys.*, vol. 162, no. 1, pp. 130–136, 2010.

[33] H. Jansen *et al.*, “A survey on the reactive ion etching of silicon in microtechnology,” *J. Micromech. Microeng.*, vol. 6, pp. 14–28, 1996.

[34] H. H, “19th Semiconductor Technology Seminar,” 1981, p. 193.

[35] Nojiri K, *Dry Etching Technology for Semiconductors*. 2015.

[36] S. McColman, “An introduction to Bosch processing on the ICPRIE.”

[37] R. Zhou, H. Zhang, Y. Hao, and Y. Wang, “Simulation of the Bosch process with a string-cell hybrid method,” *J. Micromechanics Microengineering*, vol. 14, no. 7, pp. 851–858, 2004.

[38] R. Langer, “New methods of drug delivery,” *Science (80-.).*, vol. 249, pp. 1527–1533, 1990.

[39] R. G. Crystal, “Transfer of genes to humans: early lessons and obstacles to success,” *Science (80-.).*, vol. 270, pp. 404–410, 1995.

[40] R. Shahrokh, Z., Sluzky, V., Cleland, J., Shire, S. and E. T., “Therapeutic Protein and Peptide Formulation and Delivery,” *merican Chem. Soc. Washington, DC*, 1997.

[41] M. R. Prausnitz, “Microneedles for transdermal drug delivery,” *Adv. Drug Deliv. Rev.*, vol. 56, no. 5, pp. 581–587, 2004.

[42] S. N. Mantha, “Fabrication of PPF Based Drug Containing Microneedle Arrays by Microstereolithography,” pp. 1–134, 2013.

[43] N. H. Talbot and A. P. Pisano, “Polymolding: two wafer polysilicon micromolding of closed-flow passages for microneedles and microfluidic devices,” *Tech. Dig. Solid-State Sens. Actuator Work.*, pp. 265–8, 1998.

[44] P. K. Campbell, K. E. Jones, R. J. Huber, K. W. Horch, and R. A. Normann, “A Silicon-Based, Three-Dimensional Neural Interface: Manufacturing Processes for an Intracortical Electrode Array,” *IEEE Trans. Biomed. Eng.*, vol. 38, no. 8, pp. 758–768,

1991.

[45] M., R., Prausnitz, And, R., and Langer, “Transdermal drug delivery,” *Nat. Biotechnol.*, vol. 26, pp. 1261–1268, 2008.

[46] S. Henry, “Microfabricated microneedles: A novel approach to transdermal drug delivery (vol 87, pg 922, 1998),” *J. Pharm. Sci.*, vol. 88, no. 9, p. 948, 1999.

[47] N. Roxhed, “A Fully Integrated Microneedle-based Transdermal Drug Delivery System,” KTH—Royal Institute of Technology, 2007.

[48] A. D. V. McAllsiter, F. Cros, S. P. Davis, L. M. Matta, M. R. Prausnitz and M. G. Allen, “Three-dimensional hollow microneedles and microtube arrays,” in *The 10th Int. Conf. on Solid-state Sensors and Actuators*, 1999, pp. 1098–101.

[49] B. Stoeber and D. Liepmann, “Fluid Injection Through Out-of-Plane Microneedle,” vol. 1, no. I, pp. 224–228, 2000.

[50] P. Griss and G. Stemme, “Side-opened out-of-plane microneedles for microfluidic transdermal liquid transfer,” *J. Microelectromechanical Syst.*, vol. 12, no. 3, pp. 296–301, 2003.

[51] N. Roxhed, P. Griss, and G. Stemme, “Reliable in-vivo penetration and transdermal injection using ultra-sharp hollow microneedles,” *Dig. Tech. Pap. - Int. Conf. Solid State Sensors Actuators Microsystems, TRANSDUCERS ’05*, vol. 1, pp. 213–216, 2005.

[52] H. J. G. E. Gardeniers *et al.*, “Silicon micromachined hollow microneedles for transdermal liquid transport,” *J. Microelectromechanical Syst.*, vol. 12, no. 6, pp. 855–862, 2003.

[53] “Current Patents Gazette,” 2006.

[54] Jung-Hwan Park, Yong-Kyu Yoon, M. R. Prausnitz, and M. G. Allen, “High-aspect-ratio tapered structures using an integrated lens technique,” *17th IEEE Int. Conf. Micro Electro Mech. Syst. Maastricht MEMS 2004 Tech. Dig.*, pp. 383–386, 2004.

[55] J. H. Park, Y. K. Yoon, S. O. Choi, M. R. Prausnitz, and M. G. Allen, “Tapered conical polymer microneedles fabricated using an integrated lens technique for transdermal drug delivery,” *IEEE Trans. Biomed. Eng.*, vol. 54, no. 5, pp. 903–913, 2007.

[56] S. J. M. and S. S. Lee, “A novel fabrication method of a microneedle array using inclined deep x-ray exposure,” *Micromechanics and Microengineering*, vol. 15, pp. 903–911, 2005.

[57] J. Gupta, “Microneedles for Transdermal Drug Delivery in Human Subjects - PhD Thesis,” *Design*, no. August, pp. 1–227, 2009.

[58] J. D. Brazzle *et al.*, “Fluid-coupled hollow metallic microfabricated needle arrays,” in *PROCEEDINGS OF SPIE*, 1998, no. September 1998.

[59] J. D. Brazzle, S. K. Mohanty, and a. B. Frazier, “Hollow metallic micromachined needles with multiple output ports,” in *PROCEEDINGS OF SPIE*, 1999, vol. 3877, no. August 1999, pp. 257–266.

[60] D. V. Mcallister, “MICROFABRICATED NEEDLES FOR TRANSDERMAL DRUG DELIVERY,” Georgia Institute of Technology, 2000.

[61] S. Zimmermann, D. Fienbork, B. Stoeber, A. W. Flounders, and D. Liepmann, “A microneedle-based glucose monitor: Fabricated on a wafer-level using in-device

enzyme immobilization," *TRANSDUCERS 2003 - 12th Int. Conf. Solid-State Sensors, Actuators Microsystems, Dig. Tech. Pap.*, vol. 1, pp. 99–102, 2003.

[62] L. Lin and A. P. Pisano, "Silicon-Processed Microneedles," vol. 8, no. 1, pp. 78–84, 1999.

[63] Q. B. K. D. Wise, "Single-Unit Neural Recording with Active Microelectrode Arrays," *IEEE Trans. Biomed.*, vol. Eng. 48, p. 911, 2001.

[64] WIKIPEDIA, "Deep reactive-ion etching," 2018. [Online]. Available: https://en.wikipedia.org/wiki/Deep_reactive-ion_etching.

[65] N. Chekurov, K. Grigoras, A. Peltonen, S. Franssila, and I. Tittonen, "The fabrication of silicon nanostructures by local gallium implantation and cryogenic deep reactive ion etching," *Nanotechnology*, vol. 20, no. 6, 2009.

[66] N. Chekurov, K. Grigoras, L. Sainiemi, A. Peltonen, I. Tittonen, and S. Franssila, "Dry fabrication of microdevices by the combination of focused ion beam and cryogenic deep reactive ion etching," *J. Micromechanics Microengineering*, vol. 20, no. 8, 2010.

[67] J. Parasuraman, A. Summanwar, F. Marty, P. Basset, D. E. Angelescu, and T. Bourouina, "Deep reactive ion etching of sub-micrometer trenches with ultra high aspect ratio," *Microelectron. Eng.*, vol. 113, pp. 35–39, 2014.

[68] S. L. Lai, D. Johnson, and R. Westerman, "Aspect ratio dependent etching lag reduction in deep silicon etch processes," *J. Vac. Sci. Technol. A Vacuum, Surfaces, Film.*, vol. 24, no. 4, pp. 1283–1288, 2006.